Julius-Maximilians-Universität Würzburg

Faculty of Physics and Astronomy

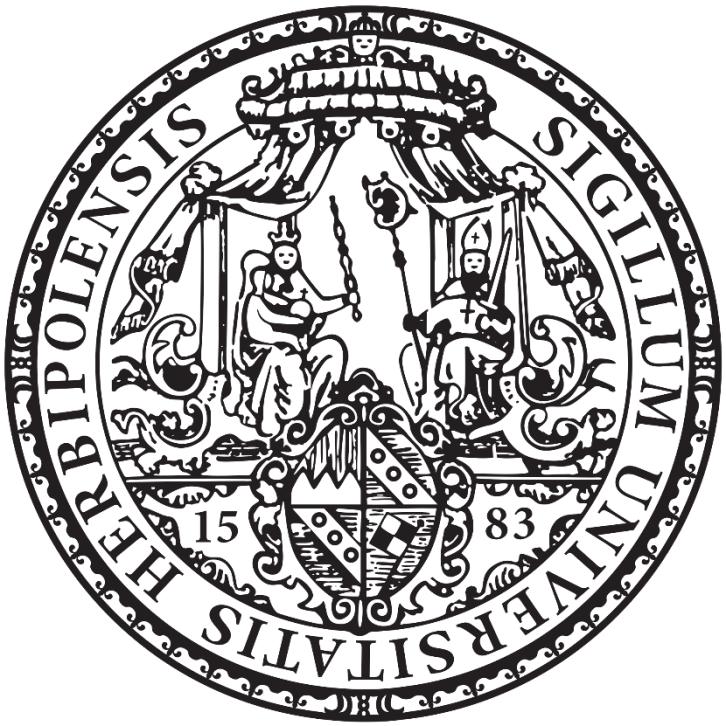

VLBI Observations of Neutrino-Candidate Blazars

A thesis submitted in fulfillment of the requirements

for the degree of Master of Science

Author: Luis Wachter

Supervisor: Prof. Dr. Matthias Kadler

Date of Submission: 26 February 2021

Zusammenfassung

Relativistische Jets in aktiven galaktischen Kernen (AGN) gehören zu den stärksten Objekten im beobachtbaren Universum. Sie emittieren Strahlung im gesamten elektromagnetischen Spektrum und werden durch die Akkretion von Materie auf ein supermassives schwarzes Loch im Zentrum ihrer Wirtsgalaxie angetrieben. Es wird angenommen, dass AGN und insbesondere Blazare auch eine Quelle für hochenergetische extragalaktische Neutrinos sind. In den letzten Jahren hat das IceCube Neutrino-Observatorium immer mehr Neutrinos entdeckt, deren Ursprung mit einem AGN zusammenfällt. Das Spine-Sheath-Modell kann die Neutrinoproduktion mit Wechselwirkungen zwischen einem sich schnell bewegenden Spine im Zentrum des Jets und einer sich langsamer bewegenden Hülle um den Spine erklären.

In dieser Arbeit werden die Neutrino-assoziierten Blazare PKS B1424-418, TXS 0506+056 und PKS 1502+106 auf Hinweise auf das Spine-Sheath-Modell in Form von Limb-Brightening des Jets oder Mustern in der Polarisation untersucht. Zu diesem Zweck werden Radiobeobachtungen, die mit der Very Long Baseline Interferometrie gewonnen wurden, ausgewertet und mit verschiedenen Stacking-Techniken untersucht.

Von PKS B1424-418 werden zehn TANAMI-Beobachtungen ausgewertet und gestapelt. Die Quelle zeigt einen hellen Kern mit einem Jet, der sich nach Nordosten ausdehnt. In einigen Epochen, wie auch im gestapelten Bild, zeigt der Jet Anzeichen von Limb-Brightening. TXS 0506+056 wird durch die Analyse von 24 archivierten MOJAVE-Beobachtungen untersucht, die auch Polarisationsinformationen enthalten. Es zeigt sich ebenfalls ein heller Kern mit einem Jet, der sich nach Süden ausdehnt sowie Hinweise auf Limb-Brightening im Jet. Das gestapelte polarisierte Bild zeigt EVPAs, die im Spine des Jets tendenziell parallel zum Jet verlaufen und in den äußeren Teilen orthogonal. PKS 1502+106 wird durch die Analyse von 28 archivierten MOJAVE-Beobachtungen untersucht. Die Quelle zeigt ebenfalls einen hellen Kern und einen nach Südosten expandierenden Jet. Limb-Brightening ist nur in wenigen Episoden schwach sichtbar. Außerdem zeigt das gestapelte Gesamtintensitätsbild kein Limb-Brightening. Das gestapelte polarisierte Bild zeigt jedoch das gleiche

Verhalten der EVPAs wie bei TXS 0506+056, was das Spine-Sheath-Modell unterstützt. Zusätzlich wird eine Beobachtung von PKS 1502+106 bei 15 GHz, 24 GHz und 43 GHz durch die Erstellung von Spektralindexkarten untersucht.

Die Entdeckung von starken Hinweisen auf Limb-Brightening und unterschiedliche Orientierungen der EVPAs in den äußeren Teilen des Jets im Vergleich zum Spine in allen drei Blazaren ist konsistent mit dem Spine-Sheath-Modell. Daher könnte dieses Modell eine Erklärung für die beobachteten IceCube-Neutrinos sein.

Abstract

Relativistic jets in active galactic nuclei (AGN) are among the most powerful objects in the observable universe. They emit radiation in the entire electromagnetic spectrum and are fueled by the accretion of matter onto a supermassive black hole in the center of their host galaxy. It is assumed that AGN, and blazars in particular, are also a source of high-energy extragalactic neutrinos. In recent years, the IceCube Neutrino Observatory has discovered more and more neutrinos with a position of origin coincident with an AGN. The spine-sheath model can explain the neutrino production with interactions between a fast-moving spine in the center of the jet and a slower moving sheath around the spine.

In this thesis, the neutrino-associated blazars PKS B1424-418, TXS 0506+056, and PKS 1502+106 are studied for hints of the spine-sheath model in the form of limb-brightening in the jet or patterns in the polarization. For this purpose, radio observations obtained with very long baseline interferometry (VLBI) are imaged and analyzed with different stacking techniques.

From PKS B1424-418, ten total intensity TANAMI observations are imaged and stacked. The source shows a bright core with a jet expanding to the north-east. In some epochs, as well as in the stacked image, the jet shows hints of limb-brightening. TXS 0506+056 is studied by imaging 24 archival MOJAVE observations that also contain polarization information. It also shows a bright core with a jet expanding south and hints of limb-brightening in the jet. The stacked polarized image shows EVPAs that tend to be parallel to the jet in the jet's spine and orthogonal in the outer parts. PKS 1502+106 is studied by imaging 28 archival MOJAVE observations. The source also shows a bright core and a jet expanding south-east. Limb-brightening is only visible weakly in few episodes. Furthermore, the stacked total intensity image shows no limb-brightening. However, the stacked polarized image indicates the same behavior of EVPAs as in TXS 0506+056, supporting a spine-sheath-model. Additionally, an observation of PKS 1502+106 at 15 GHz, 24 GHz, and 43 GHz is studied by calculating spectral index maps.

The discovery of strong hints of limb-brightening and different orientations of

EVPAs in the outer parts than the spine in all three blazars is consistent with the spine-sheath model. Therefore, this model could be an explanation for the observed IceCube neutrinos.

Contents

1. Scientific Context

1.1. Blazars as Neutrino Emitters

Since their first discovery, active galactic nuclei (AGN) have attracted the attention of astronomers of different fields. Emitting radiation at the whole electromagnetic spectrum, numerous telescopes, space probes, and other experiments went towards the exploration of these objects. With the first detections of high-energy extragalactic neutrinos by the IceCube experiment, a whole new era of multi-messenger astronomy has started. Since these first detections, evidence piles up that AGN, and blazars in particular, could play a significant role as an origin of these neutrinos. The following sections briefly introduce the currently accepted AGN model, focusing on blazars and their properties, and show how this model can describe their radio spectrum. Furthermore, an overview of the neutrino associations and previous research of the objects studied in this thesis is presented, along with a description of the so-called spine-sheath-model that could explain the neutrino flux of AGNs.

1.1.1. AGN Zoo and Unification

The discovery of AGN started in the early 20th century by observing individual phenomena, for example, the discovery of a jet in M 87 by Curtis (1918) or the detection of broad emission lines in bright nuclei of some galaxies by Seyfert (1943). Over time, more and more categories of objects were discovered until Antonucci (1993) proposed a unifying model for all AGN (see also Urry and Padovani (1995) for a review). A visual representation of this model is shown in Figure 1.1.

As proposed by Salpeter (1964), the energy source is accretion onto a supermassive black hole (SMBH) that is surrounded by the following parts: A dense accretion disc of matter measuring about $10^{-3}\,\mathrm{pc}$ followed by a broad line region (BLR) spanning from $0.01\,\mathrm{pc}$ to $0.1\,\mathrm{pc}$. The BLR consits of fast moving clouds of photoionized gas, leading to the emission of Doppler-broadened lines. A dusty torus lies at $1\,\mathrm{pc}$ up to a few $10\,\mathrm{pc}$, and a narrow line region (NLR) at $100\,\mathrm{pc}$ up to $1000\,\mathrm{pc}$. Compared

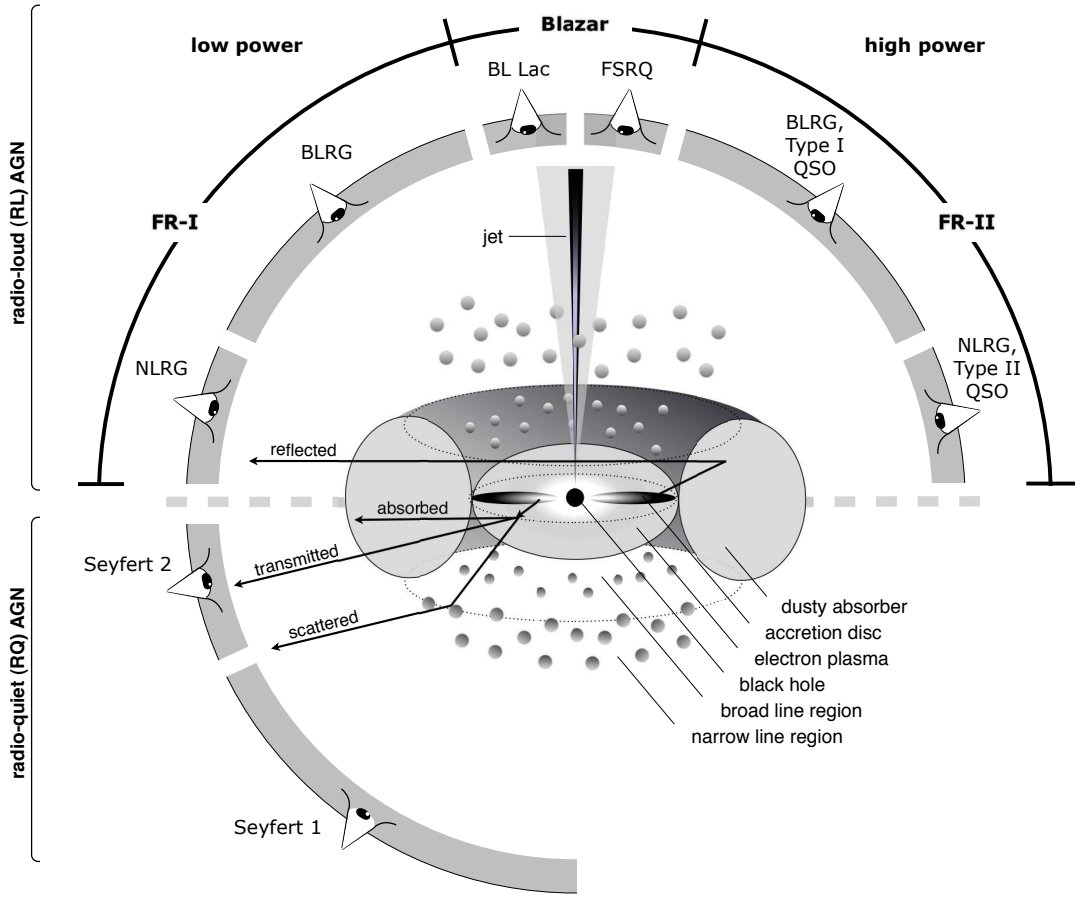

Figure 1.1.: Unification model by Beckmann and Shrader (2012). In the center, a simple AGN model with the black hole in its center is shown. The illustration is divided into radio-loud AGN in the top half and radio-quiet AGN in the bottom half. High luminosity objects are on the right, and low luminosity objects on the left. The eyes illustrate observing an AGN at different observation angles.

to the BLR, the NLR consists of colder and less dense gas clouds that emit narrow lines.

The unification model describes all different AGN only by the observer's viewing angle, the luminosity, and the radio loudness. The radio loudness R_{r-o} defined by Kellermann et al. (1989) is one of the simplest classification of AGN, where

$$R_{r-o} = \frac{S_r}{S_o}, \tag{1.1}$$

with the radio flux density S_r and the optical flux density S_o. An AGN is called radio-quiet if $0.1 < R_{r-o} < 1$ and radio-loud if $R_{r-o} > 10$. In Figure 1.1 radio-quiet AGN are in the bottom half and radio-loud in the top half. Radio-loud sources form jets perpendicular to the accretion disc in both directions that can reach lengths exceeding millions of parsecs. The right half of the figure illustrates all high luminosity AGN, and the left half the low luminosity objects.

Low luminosity, radio-quiet AGN are observed as Seyfert galaxies, which differ from non-active galaxies with their bright and point-like center. Seyfert 1 galaxies show broad allowed and narrow forbidden lines in their spectrum, resulting from the observer seeing the BLR and the NLR due to the high inclination angle. In contrast, Seyfert 2 galaxies show only narrow forbidden lines because the dusty torus blocks the sight to the broad-line region due to the low inclination angle.

Radio-loud AGN are called radio galaxies and can be subdivided into broad-line region galaxies (BLRG) and narrow-line region galaxies (NLRG), where the same principle takes place as with Seyfert 1 and Seyfert 2 galaxies. They can also be divided into low-power Fanaroff-Riley type 1 (FR-1) galaxies and high-power FR-2 galaxies. FR-1 galaxies show a bright nucleus with two jets in the radio regime that end in so-called radio plumes. In contrast, FR-2 galaxies often show only a one-sided jet and bright radio lobes where the jet hits the intergalactic medium.

If the observer is looking directly into the jet of a radio-loud AGN, a blazar is observed. These objects are compact and extremely luminous radio sources. Usually, they are subdivided according to their spectra into flat-spectrum radio quasars (FSRQ) showing broad emission lines, optically violent variables (OVV) also showing broad emission lines, and BL Lacertae objects (BL Lac objects) showing no emission lines. FSRQ are more luminous than BL Lac objects in the radio regime.

The multiwavelength spectral energy distribution (SED) of a blazer has a distinctive double-hump structure, shown in Figure 1.2 on the example of Mrk 421. The low-energy hump's origin is explained by synchrotron radiation. The high-energy

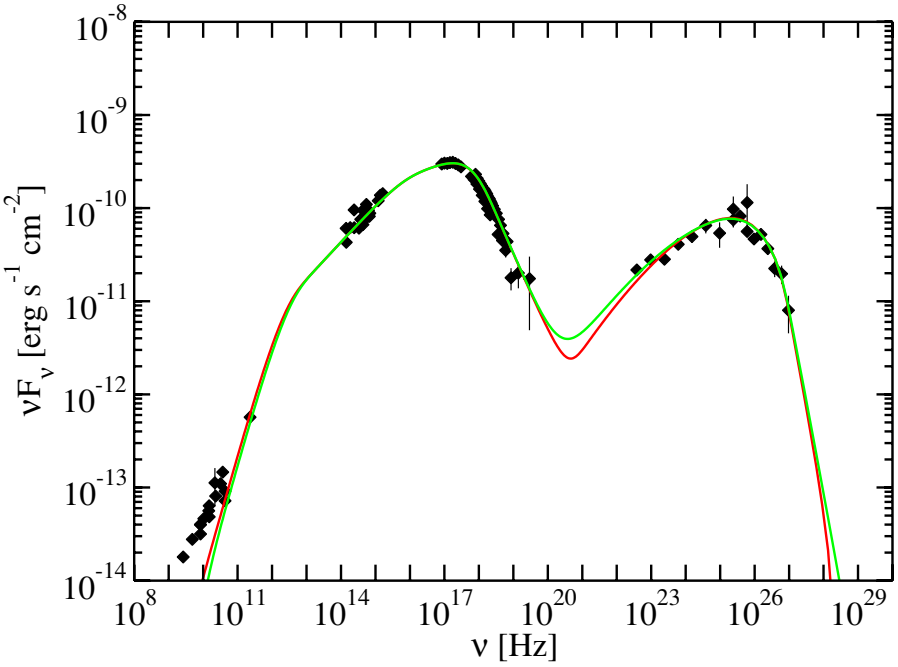

Figure 1.2.: Typical double hump structure of a blazar SED shown on the example of MRK 421. Shown in green and red are two different fits of a one-zone SSC model. Taken from Abdo et al. (2011).

hump is not yet fully understood, and there are purely leptonic and lepto-hadronic models to describe it. Leptonic models are based on inverse Compton scattering by the same electrons emitting the synchrotron radiation of the low-energy hump. However, several sources of the target photons are debated, such as synchrotron self-Compton (SSC) or external Compton (EC) mechanisms. The radio-spectrum of blazars is a steep power-law in lower radio frequencies and mostly flat in higher frequencies. How this spectrum is formed is explained in detail in the next section.

1.1.2. Blazar Emission

To understand and model the typical spectrum of blazars in the radio regime, the concept of synchrotron radiation is needed and will be explained following Rybicki and Lightman (1979).

Any particle holding a charge q that is exposed to an electromagnetic field will experience the Lorentz force

$$\vec{F_L} = q\left(\vec{E} + \vec{\beta} \times \vec{B}\right) \tag{1.2}$$

in which $\vec{\beta} = \vec{v}/c$ is the velocity of the particle in units of the speed of light. Here, the case of an electron of charge e and mass m_e only exposed to an magnetic field $\vec{B}$ is explored and the motion of it can be described with

$$\frac{d}{dt}(\gamma\, m\vec{v}) = \frac{e}{c}\left(\vec{v} \times \vec{B}\right), \tag{1.3}$$

in which $\gamma = (1-\beta^2)^{-1/2}$ is the Lorentz-factor. In this case, the electron will perform a helical motion around a $\vec{B}$ field line with the characteristic frequency of $\omega_B = \frac{eB}{\gamma m_e c}$, provided that $\vec{B}$ is linear. This frequency is equal to the Larmor frequency.

All charged particles accelerated radially emit electromagnetic radiation and the emitted power P is given by Larmor's formula

$$P = \frac{dE}{dt} = \frac{q^2\dot{v}^2}{4\pi c^3}\int sin^2\theta\, d\Omega = \frac{2q^2\dot{v}^2}{3c^3}. \tag{1.4}$$

Note that E is here the energy, not the electric field $\vec{E}$.

With the assumptions of an isotropic velocity distribution and highly relativistic electrons, the average emitted power $\langle P\rangle$ of the electron can be calculated to

$$\langle P\rangle = \frac{4}{3}\beta^2\,\gamma^2\,c\,\sigma_T\,u_B \tag{1.5}$$

in which $\sigma_T = (8\pi e^2)/(3m^2c^4)$ is the Thomson cross section and $u_B = B^2/(8\pi)$ the magnetic field energy density. Note that $\langle P\rangle \propto \sigma_T \propto m_e^{-2}$, which shows that radiation from heavy charged particles (like protons) can be neglected.

For an electron distribution with the electron energy density $n(\gamma)$, the emitted spectrum is given by

$$P_\nu = \int_1^\infty P_\nu(\gamma)\, n(\gamma)\, \mathrm{d}\gamma, \tag{1.6}$$

in which the contribution of electrons with different energies is weighted. Assuming non-thermal synchrotron radiation, where electrons follow the power-law distribution

$$n(\gamma)\,\mathrm{d}\gamma = n_0\,\gamma^{-p}\,\mathrm{d}\gamma, \tag{1.7}$$

the spectral energy distribution P_ν can be written as

$$P_\nu = \frac{4}{3}\,\beta^2\,\gamma^2\,c\sigma_T\,U_B\,\phi_\nu(\gamma). \tag{1.8}$$

$\phi_\nu(\gamma)$ is the spectral shape with the property of $\int \phi_\nu(\gamma)\,\mathrm{d}\nu = 1$.

With the assumption of electrons emitting only at a characteristic frequency of $\omega_c = \gamma^2\omega_L = \frac{eB}{m_e c}\left(\frac{E}{m_e c^2}\right)^2$ with the Larmor-frequency ω_L, the spectral shape is described by a Dirac-δ function:

$$\phi_\nu(\gamma) \sim \delta(\nu - \omega_c). \tag{1.9}$$

Then, the superposition of all individual electron spectra follows a power-law which can be calculated to

$$P_\nu = \frac{2}{3}\,c\,\sigma_T\,n_0\,\frac{u_B}{\nu_L}\left(\frac{\nu}{\nu_L}\right)^{-\frac{p-1}{2}}. \tag{1.10}$$

Note that $P_\nu \propto \nu^{-\alpha}$, in which $\alpha = \frac{p-1}{2}$ is called the spectral index.

However, the derived emitted spectrum occurs only in a thin optical environment, where the optical depth $\tau_\nu < 1$. The optical depth is given by $\tau_\nu = \int_s \alpha^s \alpha_\nu(s')\,\mathrm{d}s'$, in which s is the traveled distance through the medium and α_ν is the absorption coefficient. If the environment is optical thick ($\tau_\nu \gg 1$), synchrotron self-absorption (SSA) takes place, where the electrons absorb their own emitted photons. Then, the spectrum follows a power-law of $P_\nu \propto \nu^{5/2}$ independent of p. Since the optical depth is heavily dependent on the frequency ν, this leads to a spectrum of $P_\nu \propto \nu^{5/2}$ for low frequencies and $P_\nu \propto \nu^{-\alpha}$ for the high frequencies with a spectral turnover at $\tau_\nu = 1$. Note that $\tau_\nu \propto R$, in which R is the size of the emitting region.

Consider now a conical jet with several emitting regions, also called blobs, that are different in size, as shown in Figure 1.3. Because the blobs are different in size, the turnover frequency of the synchrotron spectrum shifts for each region, resulting in a flat radio spectrum. In the lower end of the spectrum, unbeamed emission from optical thin regions like radio-lobes dominates, resulting in a steep spectrum.

Because the emitting electrons are highly relativistic, a potential observer of a blazar looking almost directly into the jet experiences an effect called relativistic beaming (Cohen et al. 2007). This effect leads to an enhanced observed luminosity of $L = L_0\delta^{\alpha+p}$, in which L_0 is the intrinsic, unbeamed luminosity, α the spectral index and p a jet geometry depandent index. δ is the Doppler factor of the electrons given

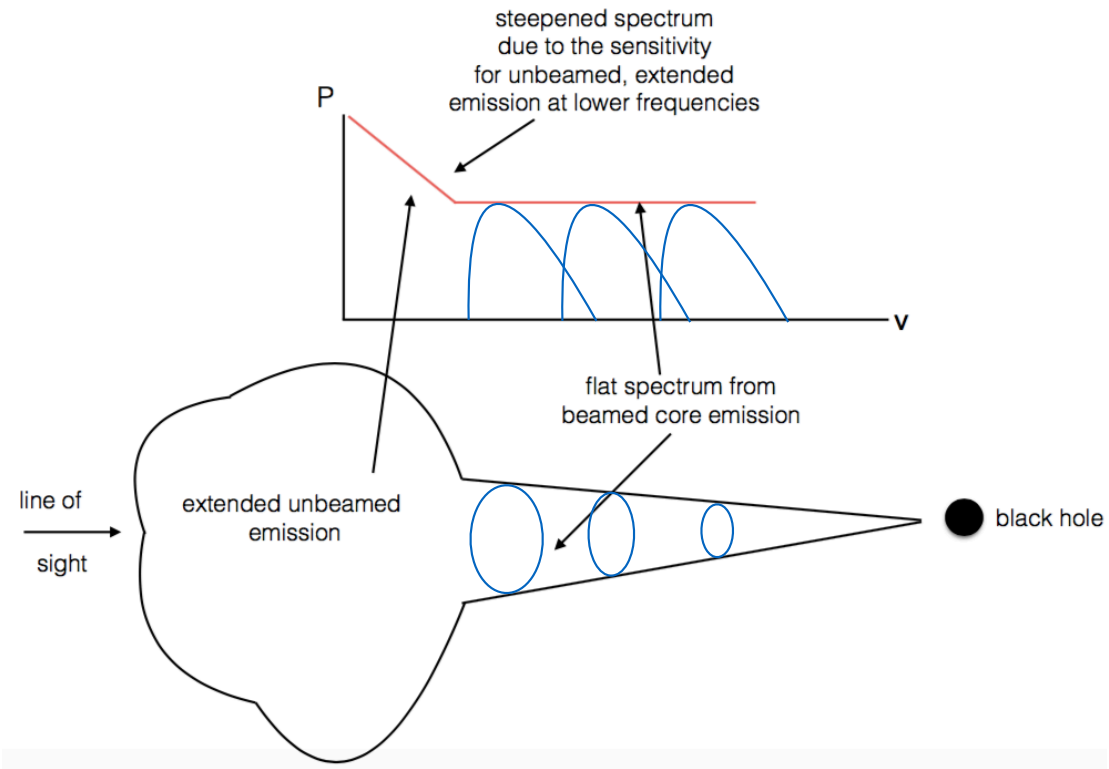

Figure 1.3.: The radio spectrum of a blazar. The observer looks directly in the jet. The spectrum is composed of the unbeamed emission regions producing a steep power-law spectrum in the low radio frequencies and the beamed emission of the jet's many emission regions producing a flat spectrum in higher radio frequencies. Adapted from Burd (2017).

by

$$\delta = \frac{1}{\gamma\,(1 - \beta\,cos\theta)}, \tag{1.11}$$

in which β is the velocity of the electrons in units of c and θ the observation angle. Considering a blazar with a jet moving towards the observer and a jet moving in the opposite direction, relativistic beaming leads to severe consequences regarding the blazar's appearance. Flux emitted by the jet moving towards the observer is beamed to higher values, while the opposite jet's flux is beamed to lower values. In the case of a blazar, in which the angle to the line of sight is extremely small, the difference in observed flux density can reach extreme values. Therefore, blazars often show only a one-sided jet, where the counterjet is invisible due to the difference in apparent flux density between both sides of the jet.

1.1.3. The Structured Neutrino Blazar

In the early 2000s, several VLBI studies like Giroletti et al. (2004) showed that the jets of powerful TeV BL Lac objects are moving more slowly than other types of sources. These observations challenged currently accepted jet-models: To produce this strong TeV emission, a highly relativistic jet is needed for the TeV emission not to be absorbed by the jet's infra-red (IR) emission. This was also backed up by modeling SEDs of these objects with one-zone SSC models that lead to Doppler factors of 10 to 50 (e.g., Tavecchio and Maraschi 2001, Krawczynski et al. 2002), which was not compatible with the observation of slow-moving jets. One possibility to resolve these contradictions was the idea of an extreme deceleration of the jet between the region responsible for the TeV emission and the jet observed in VLBI. Georganopoulos and Kazanas (2003) showed that this type of radially structured jet enhances the inverse Compton emission. This lowers the needed Doppler factors for the strong TeV emission in a one-zone SSC model. The enhancement takes place if the entire TeV zone is decelerating. Then, the fast-moving base sees the radiation of the slow-moving end relativistically boosted, which leads to the enhancement of inverse Compton emission.

Ghisellini et al. (2005) proposed a different kind of jet model, in which the jet is not structured radial but transverse. In their model, the jet is derived of a fast-moving cylindrical spine in the center and a slow-moving hollow cylinder around the spine called the layer or sheath (see Figure 1.4 for a visual representation of the model).

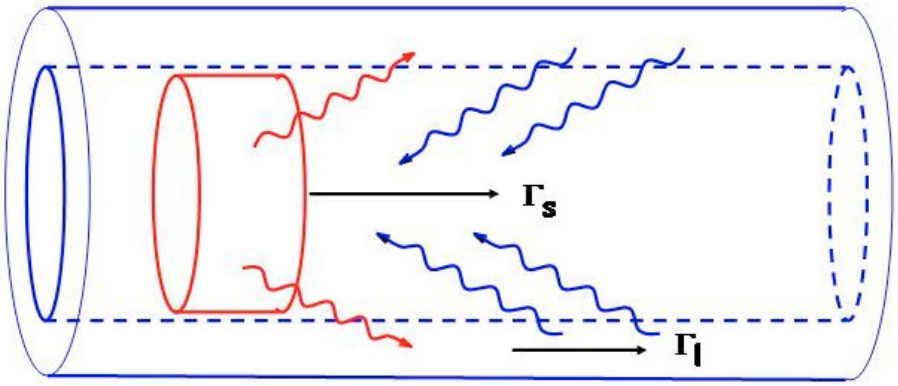

Figure 1.4.: Spine-sheath model by Ghisellini et al. (2005). The fast moving spine is moving with a Lorentz factor of Γ_s a sees the boosted radiation of the layer. Similarly, the slow moving layer is moving with a Lorentz factor of $\Gamma_l < \Gamma_s$ and sees the boosted radiation of the spine.

This model can explain the jet's declaration in certain zones (here the slow-moving layer) with the interaction of the jet's outer parts with the stationary surrounding medium. Both structures emit radiation produced via synchrotron radiation and the inverse-Compton effect. The seed photons for the inverse-Compton effect in the spine come from the spine itself, but also the layer. Moreover, because the layer moves with a different Lorentz factor, its radiation is boosted in the spine's frame. The same is happening for the layer that sees the radiation from the spine boosted. This vital feedback enhances the inverse-Compton effect in both structures and explains the observed TeV emission in slow-moving BL Lac objects. The original model was developed only for high-peaked BL Lac objects (HBL); however, most TeV BL Lacs also seem to be HBL.

This model is also motivated by observations: Giroletti et al. (2004) found evidence of so-called limb-brightening in VLBI observations of Mrk 501, where the outer parts of the jet, the limbs, are brighter than the inner parts from a certain distance to the radio-core (also mentioned by Giovannini et al. (1999) and seen in Figure 1.5). Aaron (1999) also noted that the polarization of Mrk 501 shows hints to this layered structure with the spine having magnetic field vectors orthogonal to the jet and the edges of the jet showing magnetic field vectors parallel to the jet.

A question similar to the origin of the strong TeV emission in BL Lac objects arose when a number of these objects were linked to high-energy IceCube neutrino events by Padovani and Resconi (2014). As shown by Murase et al. (2014) and Dermer et al. (2014), the neutrino output of AGN through photo-meson production should be dominated by FSRQ that are more powerful than BL Lac objects. In

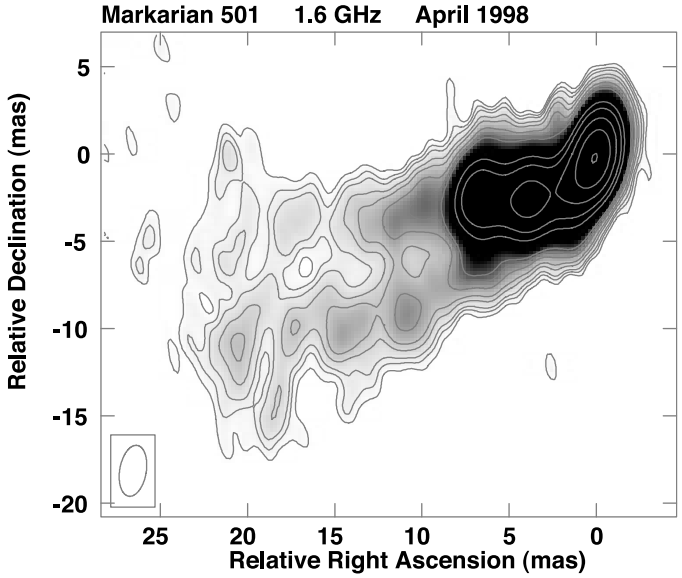

Figure 1.5.: VLBI observation of Mrk 501 by Giroletti et al. (2004). The jet is limb-brightened.

BL Lac objects, efficient neutrino production is hindered by the jet's low intrinsic power and the low radiation energy density. Murase et al. (2014) also noted that the neutrino spectrum of a simple one-zone model with a cosmic-ray source and target photons from the accretion-disk, BLR, and IR dust emission should peak above 10 PeV. IceCube data, however, does not show this behavior.

This discrepancy led Tavecchio et al. (2014) to propose the same model as reported in Ghisellini et al. (2005) as an efficient neutrino production in BL Lac objects. Here, the production of neutrinos in a photo-meson reaction is fueled by high-energy protons in the spine. The photo-meson, here a pion, decays and produces neutrinos as shown in Tavecchio et al. (2014), where no distinction between ν and $\bar{\nu}$ is made:

$$\pi^{\pm} \longrightarrow \mu^{\pm} + \nu_{\mu} \longrightarrow e^{\pm} + 2\nu_{\mu} + \nu_{e}. \tag{1.12}$$

This production is boosted similarly to the TeV photon production. Here, the neutrino production is boosted by the amplification of the layer's photon field due to the difference in Lorentz factors. Ghisellini et al. (2005) calculated the expected neutrino events from a source like Mkn 421 and Mkn 501 between one and four in a three-year exposure in agreement to Padovani and Resconi (2014). While also only developed for HBL, Tavecchio et al. (2014) also noted that a structured jet in the form of a spine and layer could lead to an essential contribution to the neutrino flux of other BL Lac objects and FSRQ as well.

1.1.4. Blazar-Neutrino Associations

In this thesis, the three blazars PKS B1424-418, TXS 0506+056, and PKS 1502+106 are studied, and introduced in this section. All of them have a strong IceCube neutrino association. Table 1.1 lists all of them, together with their redshift, the currently accepted classification, the associated IceCube event, and the reference to each association.

Name	Redshift z	Classification	IceCube Event (Association Reference)
PKS B1424-418	1.522[1]	FSRQ	HESE-35 (Kadler et al. 2016)
TXS 0506+056	0.3365[2]	BL Lac	170922A (IceCube Collab. et al. 2018b)
PKS 1502+106	1.8385[3]	FSRQ	190730A (Taboada and Stein 2019)

Table 1.1.: The blazar sample of this thesis. Redshift references: [1] White et al. (1988), [2] IceCube Collaboration et al. (2018b), [3] Abdo et al. (2010).

IceCube is a neutrino detector located at the south pole designed to observe high energy cosmic neutrinos (see Aartsen et al. (2017) for a detailed description). IceCube uses the fact that neutrino interactions produce particles that move faster through ice than the phase velocity of light and thus emit Cherenkov radiation. Buried in the thick ice are 5160 *Digital Optical Modules* (DOM), which can observe these Cherenkov photons using a photomultiplier tube. The DOMs are located at a depth between 1450 m and 2450 m under the ice's surface, covering a volume of roughly one cubic kilometer. By measuring the different arrival times of the Cherenkov photons, the path of the light-emitting particles through the detector, and, therefore, also for the neutrino can be reconstructed. A representation of a measurement of a neutrino can be seen in Figure 1.6.

This is, however, only true for track-like events found for ν_μ charged-current (CC) interactions and a minority of ν_τ CC interactions, where a high-energy muon is produced that leaves a visible track. In most events, the produced particles travel only small distances, and the particle shower is observed only in one region of the detector, not along a path. The region on the sky from where the neutrino originated can be limited to a few deg^2 for track-like events but only to several hundred deg^2 for the majority of events. In the first three years, IceCube detected 37 events with energies between 30 TeV and 2 PeV (Aartsen et al. 2014). Two of these are associated with PKS B1424-418 and TXS 0506+056.

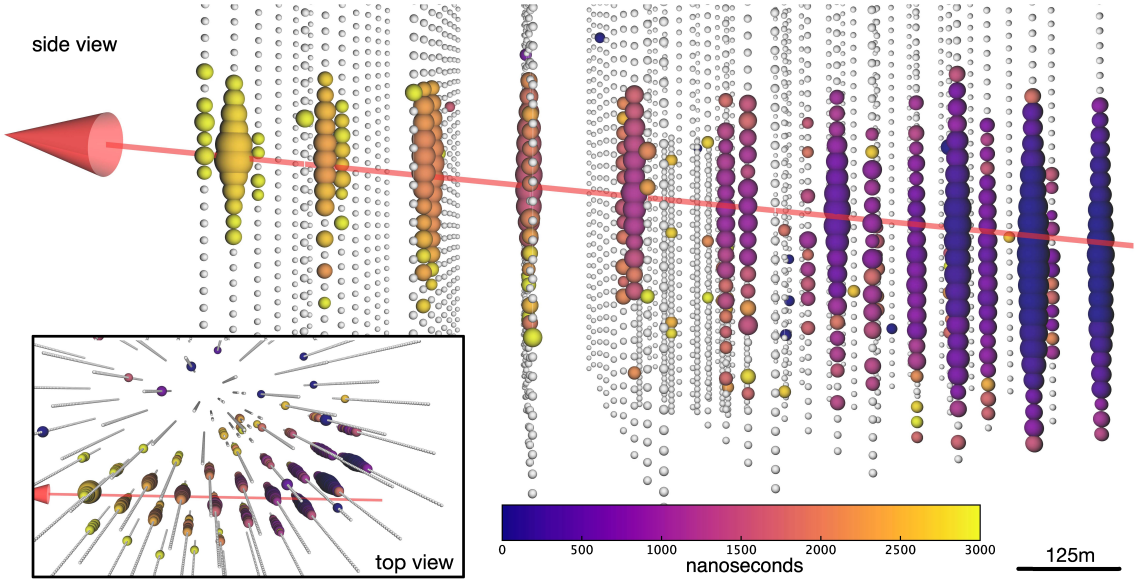

Figure 1.6.: IceCube event 170922A. Each grey and colored sphere corresponds to one DOM. Shown in color is the time of the observation of a signal by a DOM. Blue are the earliest hits, and yellow the latest. The sphere's size is proportional to the logarithm of the amount of light observed, while the total charge recorded is ~5800 photoelectrons. The arrow shows the best fit for the track direction. Image taken from IceCube Collaboration et al. (2018a).

PKS B1414-418

On 4 December 2012, IceCube detected a neutrino event with an energy of 2 PeV called HESE-35 (dubbed 'BigBird'), as reported in Aartsen et al. (2014). The IceCube analysis focused on very high energy events, where the interaction signatures are fully contained in the detector volume (high-energy starting events; HESEs). This led to a high positional uncertainty of 10° to 20°. Inside the HESE-35 field lie a total of 20 γ-ray bright AGN, based on observations with the Fermi/LAT space telescope between August 2008 and September 2010, as reported in Kadler et al. (2016). PKS B1424-418 is the dominant blazar in this field but was previously ruled out as a counterpart to the HESE-35 event by Padovani and Resconi (2014) due to its low γ-ray flux between 2008 and 2011. However, in 2012 started a high-fluence outburst lasting more than one year as shown in Figure 1.7. The figure also shows the arrival time of HESE-35.

Between July 2012 and 2013 PKS B1424-418 even showed the highest γ-ray fluence between 100 MeV and 300 GeV of all extragalactic sources. An increase in X-ray, optical, and radio emission was also seen. Figure 1.7 shows three TANAMI images observed at 8.4 GHz, which show an increase from $\sim$ 1.5 Jy beam^{-1} to $\sim$ 6 Jy beam^{-1}

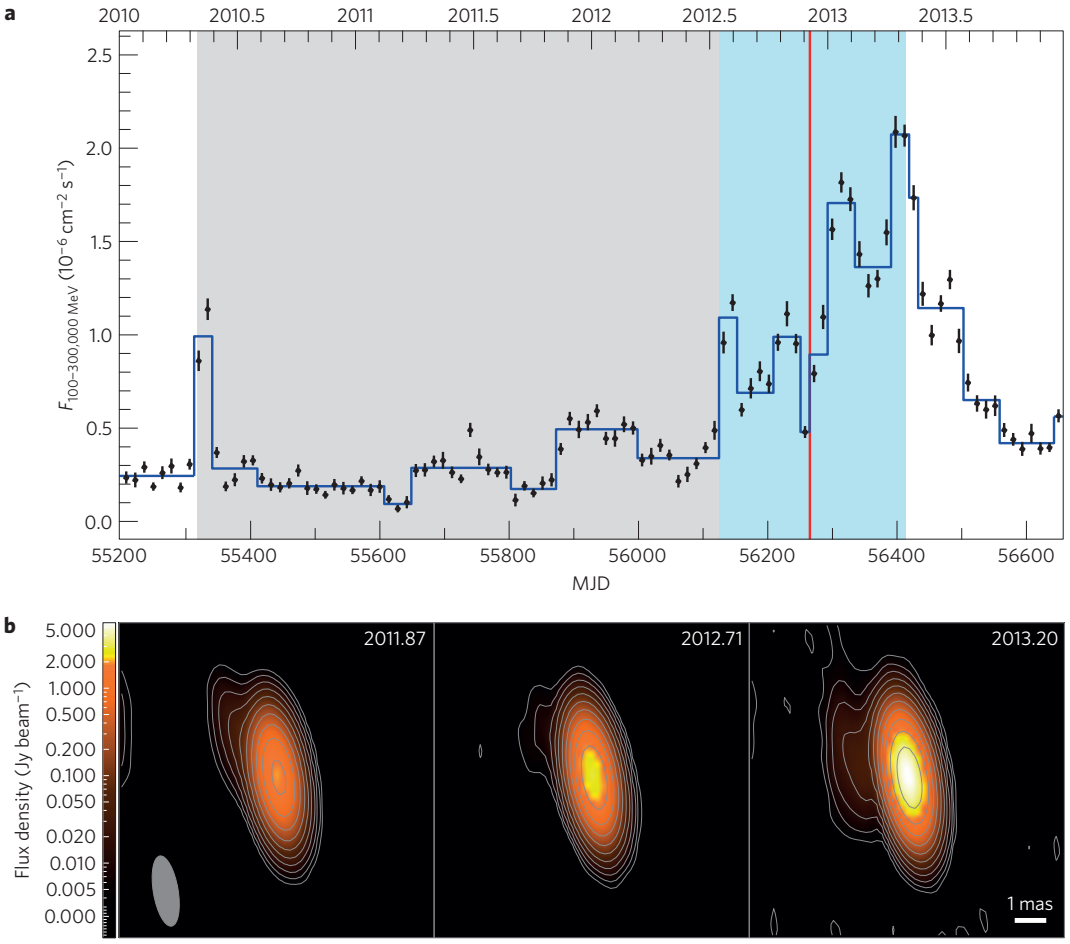

Figure 1.7.: Top: Fermi/LAT lightcurve for PKS B1424-418 with two-week binned photon fluxes between 100 MeV and 300 GeV. Shown in red is the date of the HESE-35 event, and in color the total HESE period, as well as the outburst time range. Bottom: TANAMI images of PKS B1424-418 with an increase in peak flux density from 1.95 Jy beam^{-1} to 5.62 Jy beam^{-1}. Image taken from Kadler et al. (2016).

in radio flux density in the core. Kadler et al. (2016) showed that the chance coincidence of the neutrino event and the blazar outburst is only 5%. During the high-fluence phase, the contribution to a predicted neutrino production rate for PKS B1424-418 was more than five times higher than the contribution of all other Fermi/LAT detected blazars in the field together. In conclusion, Kadler et al. (2016) suggested that a direct physical association is justified.

TXS 0506+056

The second blazar, TXS 0506+056, is associated with the IceCube event 170922A. It was detected on 22 September 2017 and the reported neutrino energy by IceCube

Collaboration et al. (2018a) is ~ 290 TeV. Compared to the neutrino event of PKS B1424-418, IceCube-170922A is a track-like event. A visual representation of the event in the IceCube detector can be found in Figure 1.6. Therefore, the positional region of the neutrino's origin is much smaller and the 90% confidence region is only $0.97\,\mathrm{deg}^2$, and the 50% confidence region only $0.15\,\mathrm{deg}^2$. TXS 0506+056 was in a flaring state as observed by the Fermi/LAT telescope at the time of the neutrino event, and IceCube Collaboration et al. (2018a) reported a correlation between the neutrino event and the γ-flare at a 3σ confidence level. The source also shows a steep increase in radio flux starting around 2017, which increased to an all-time high at 15 GHz in 2020. These measurements were done by the OVRO 40 meter telescope[1] and the lightcurve is shown in Figure 1.8.

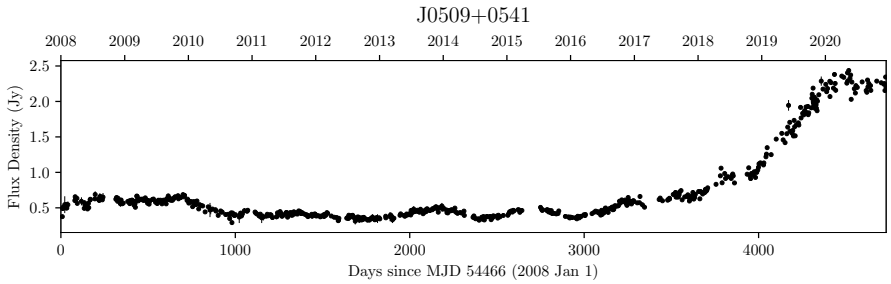

Figure 1.8.: Public OVRO lightcurve of TXS 0506+056 at 15 GHz. From `https://sites.astro.caltech.edu/ovroblazars/data.php?page=data_return&source=J0509+0541`.

In an investigation of 9.5 years of IceCube observations, an excess of high-energy neutrino events was found at a position coincident with TXS 0506+056 between September 2014 and March 2015 (IceCube Collaboration et al. 2018b). This led to a 3.5σ evidence for neutrino emission from the direction of TXS 0506+056. This association is independent of the IceCube-170922A event, making the association of the blazar to neutrino emission even stronger.

Ros et al. (2020) performed observations of TXS 0506+056 at 43 GHz with the VLBA two and eight months after the neutrino event. The two observations can be seen in Figure 1.9. A bright core with a jet is visible, where the jet is originally very collimated but expands rapidly beyond ~ 0.5 mas from the core. This is a sign of deceleration happening in the jet. Additionally, signs of limb-brightening are visible and shown in Figure 1.9 with two surface brightness profiles of the jet. This jet

[1] See Richards et al. (2011) for more information about the OVRO 40 m Telescope Monitoring Program.

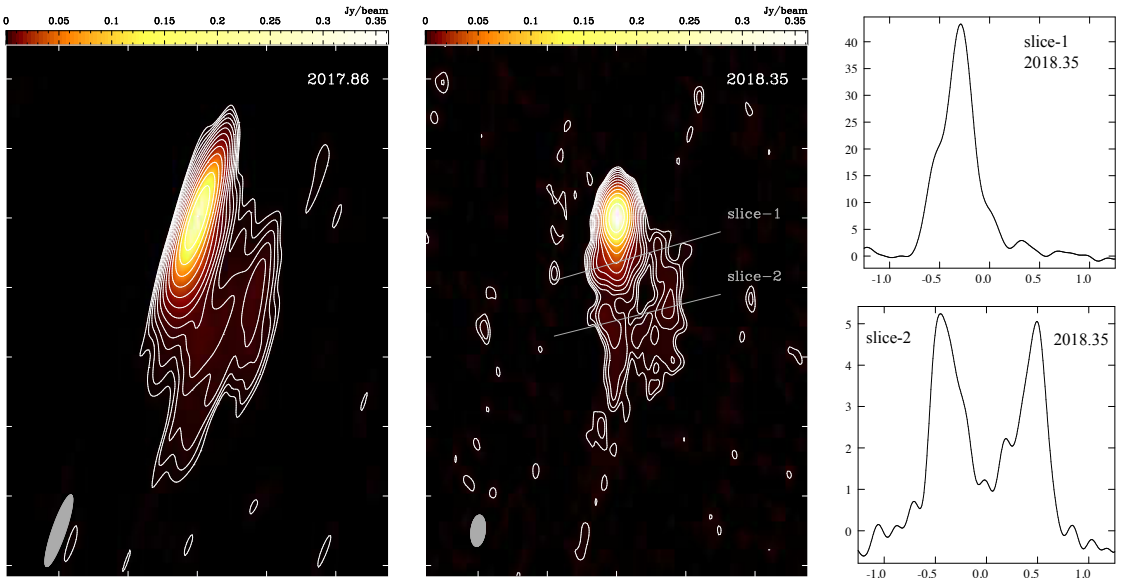

Figure 1.9.: VLBA images of TXS 0506+056 at 43 GHz observed with the VLBA two and eight months after the IceCube event 170922A. The right panels show surface brightness profiles for two slices through the jet, indicated in the middle panel. From Ros et al. (2020).

morphology is consitent with the spine-sheath model of Ghisellini et al. (2005) and Tavecchio et al. (2014) explained in Section 1.1.3.

There are also alternative explanations for the origin of the neutrino. Britzen et al. (2019) proposed that the neutrino emission results from the collision of two jets in the source. The bend in the jet of TXS 0560+056 supports this theory. However, Britzen et al. (2019) also conclude that TXS 0506+056 would need to be a special blazar for this scenario, but other studies showed that neutrino associated sources do not take a special place in their blazar sample (see Weber 2020 and Hovatta et al. 2020)

PKS 1502+106

The third blazer in the sample of this thesis, PKS 1502+106, is associated with the neutrino event IceCube-190730A, as reported in Taboada and Stein (2019). PKS 1502+106 is located within the 50% uncertainty region of the IceCube event. While the source showed no flaring activity as observed by Fermi/LAT, Kiehlmann et al. (2019) reported that it shows a long-term outburst in flux density measured at 15 GHz with the OVRO 40 meter Telescope. This outburst started in 2014 and reached an all-time high of ~ 4 Jy at the time of the neutrino event. The OVRO 40

meter telescope lightcurve is shown Figure 1.10.

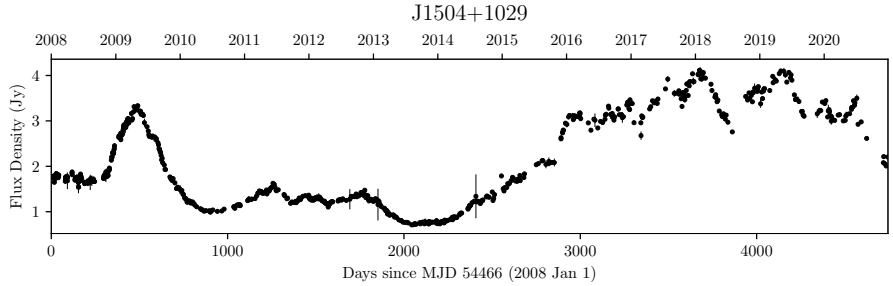

Figure 1.10.: Public OVRO lightcurve of PKS 1502+106 at 15 GHz. From `https://sites.astro.caltech.edu/ovroblazars/data.php?page=data_return&source=J1504+1029`.

1.2. Very Long Baseline Interferometry

Despite their enormous size, simple single dish radio telescopes are limited by the Rayleigh criterion in regard to their angular resolution Θ which is given by

$$\Theta \approx \frac{\lambda}{D}. \tag{1.13}$$

λ is the wavelength of the observed light and D the diameter of the telescope. Large radio telescopes like the 100 m Effelsberg Radio Telescope observing at a frequency of 15 GHz corresponding to a wavelength of 2 cm achieve an angular resolutions of ~0.69 arcmin, which is not high enough to resolve the innermost jets of blazars. This is where radio interferometry comes in, where the observations of several telescopes are synchronized and then get correlated. For a radio interferometer, the angular resolution is determined by the longest distance between two of the involved telescopes, the baseline. In a compact array like the Karl G. Jansky Very Large Array (VLA), these baselines can reach up to tens of kilometers. When utilizing radio stations that are not directly connected and separated up to thousands of kilometers, the technique is called very long baseline interferometry (VLBI). The longest baseline of the VLBA is ~6800 km, which leads to an angular resolution of ~0.61 milliarcsec (mas) at 15 GHz according to Equation 1.13. All observations in this thesis were obtained with VLBI instruments. This section will explain the basics of radio interferometry following Clark (1999) and the textbook of Burke and Graham-Smith (2009). Furthermore, the two used instruments, the VLBA and TANAMI, are introduced.

Figure 1.11 shows the simplest radio interferometer consisting of two radio an-

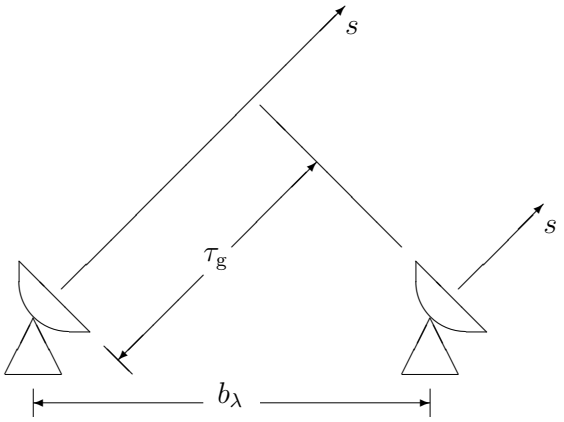

Figure 1.11.: A two element radio interferometer after Burke and Graham-Smith (2009). Two dishes are separated by the baseline $\vec{b}_\lambda$ and observe an object in the direction of $\vec{s}$. The data reaches the second antenna with a geometrical delay τ_g.

tennas. To understand the measurements of a radio interferometer, a radio source at location $\vec{R}$ emitting an electromagnetic wave with an electric field of $\vec{E}(\vec{R}, t)$ is considered. This field can be detected by the antenna at location $\vec{r}$. Because the time interval of the electric field variations is finite, $\vec{E}(\vec{R}, t)$ can be described by the real part of a Fourier series with exponentials as the time-dependent part. Then, the Fourier coefficients $\vec{E}_\nu(\vec{R})$ are used to describe the electric field. A propagater $P_\nu(\vec{R}, \vec{r})$ describes the relationship between $\vec{E}(\vec{R}, t)$ and $\vec{E}(\vec{r}, t)$. The electric field at the observer is then described by

$$\vec{E}_\nu(\vec{r}) = \iiint P_\nu\left(\vec{R}, \vec{r}\right)\ \vec{E}\left(\vec{R}, t\right)\ \mathrm{d}x\,\mathrm{d}y\,\mathrm{d}z. \tag{1.14}$$

By ignoring all polarization properties, the electric field can be described as a scalar field. It is also assumed that the observed sources are two-dimensional objects on the celestial sphere, leading to the surface brightness $\varepsilon_\nu(\vec{R})$ of the source that is observed at a distance $|\vec{R}|$. Furthermore, because the electromagnetic wave is traveling trough an emty space between $\vec{R}$ and $\vec{r}$, the propagater can described by

$$P_\nu\left(\vec{R}, \vec{r}\right) = \frac{e^{2\pi i \nu \left|\vec{R}-\vec{r}\right|/c}}{\left|\vec{R}-\vec{r}\right|} \tag{1.15}$$

leading to

$$E_\nu(\vec{r}) = \int \varepsilon_\nu\left(\vec{R}\right) \frac{e^{2\pi i \nu \left|\vec{R}-\vec{r}\right|/c}}{\left|\vec{R}-\vec{r}\right|} \mathrm{d}S, \tag{1.16}$$

in which $\mathrm{d}S$ is an infinitesimal surface area of the celestial sphere.

The spatial coherence function $V_\nu(\vec{r}_1, \vec{r}_2)$ gives the correlation of the electric field at the two positions $\vec{r}_1$ and $\vec{r}_2$ (the positions of two radio antennas) and is defined as the expectation value $\langle E_\nu(\vec{r_1}), E_\nu^*(\vec{r_2})\rangle$

$$V_\nu(\vec{r}_1, \vec{r}_2) = \left\langle \iint \varepsilon_\nu\left(\vec{R_1}\right) \varepsilon_\nu^*\left(\vec{R_2}\right) \frac{e^{2\pi i \nu \left|\vec{R}_1-\vec{r}_1\right|/c}}{\left|\vec{R}_1-\vec{r}_1\right|} \frac{e^{2\pi i \nu \left|\vec{R}_2-\vec{r}_2\right|/c}}{\left|\vec{R}_2-\vec{r}_2\right|} \mathrm{d}S_1\, \mathrm{d}S_2 \right\rangle. \tag{1.17}$$

By assuming that the radiation from the object is not spatially coherent, one yields $\langle \varepsilon_\nu(\vec{R_1}), \varepsilon_\nu^*(\vec{R_2})\rangle = 0$ for $\vec{R_1} \neq \vec{R_2}$, which leads to $\vec{R_1} = \vec{R_2}$ in Equation 1.17 and thus

$$V_\nu(\vec{r}_1, \vec{r}_2) = \int \left\langle \left|\varepsilon_\nu\left(\vec{R}\right)\right|^2 \right\rangle \left|\vec{R}\right|^2 \frac{e^{2\pi i \nu \left|\vec{R}-\vec{r}_1\right|/c}}{\left|\vec{R}-\vec{r}_1\right|} \frac{e^{2\pi i \nu \left|\vec{R}-\vec{r}_1\right|/c}}{\left|\vec{R}-\vec{r}_1\right|} \mathrm{d}S. \tag{1.18}$$

With the unitvector $\vec{s} = \vec{R}/|\vec{R}|$, the observed intensity $I_\nu(\vec{s}) = |\vec{R}|^2\langle|\varepsilon_\nu(\vec{R})|^2\rangle$, and the assumption of $\vec{R} \gg \vec{r}_i$ leading to $\mathrm{d}S = |\vec{R}|^2\mathrm{d}\Omega$, Equation 1.18 reads

$$V_\nu(\vec{r}_1, \vec{r}_2) = \int I_\nu(\vec{s})\, e^{-2\pi i \nu \vec{s}(\vec{r}_1-\vec{r}_2)/c}\, \mathrm{d}\Omega. \tag{1.19}$$

It is convenient to introduce new coordinates as shown in Figure 1.12. The vectors $\vec{r}_i$ are described in (u, v, w) and the vector $\vec{s}$ in (l, m, n). It can be shown that this leads to an infinitesimal solid angle of $\mathrm{d}\Omega = \frac{\mathrm{d}l\,\mathrm{d}m}{n} = \frac{\mathrm{d}l\,\mathrm{d}m}{\sqrt{1-l^2-m^2}}$.

By assuming the radio antennas to be coplanar, the baseline measured in wavelenghts λ is given by $\vec{b}_\lambda = \vec{r}_1 - \vec{r}_2 = \lambda(u, v, 0)^T$ and the unit vector is given by $\vec{s} = (l, m, \sqrt{1-l^2-m^2})^T$. This leads to

$$V_\nu(u, v, w) = \iint \frac{I_\nu(l, m)}{\sqrt{1-l^2-m^2}} e^{-2\pi i(ul+vm)}\, \mathrm{d}l\, \mathrm{d}m. \tag{1.20}$$

By shifting the coordinate system such that $\vec{b}_\lambda = \vec{r}_1 - \vec{r}_2 = \lambda(u, v, w)^T$ and $\vec{s}_0 = (0, 0, 1)^T \perp \sigma$, the shifted coherence function reads

$$V_\nu^S(u, v, w) = e^{2\pi i w} \iint I_\nu(l, m) e^{-2\pi i(ul+vm)}\, \mathrm{d}l\, \mathrm{d}m. \tag{1.21}$$

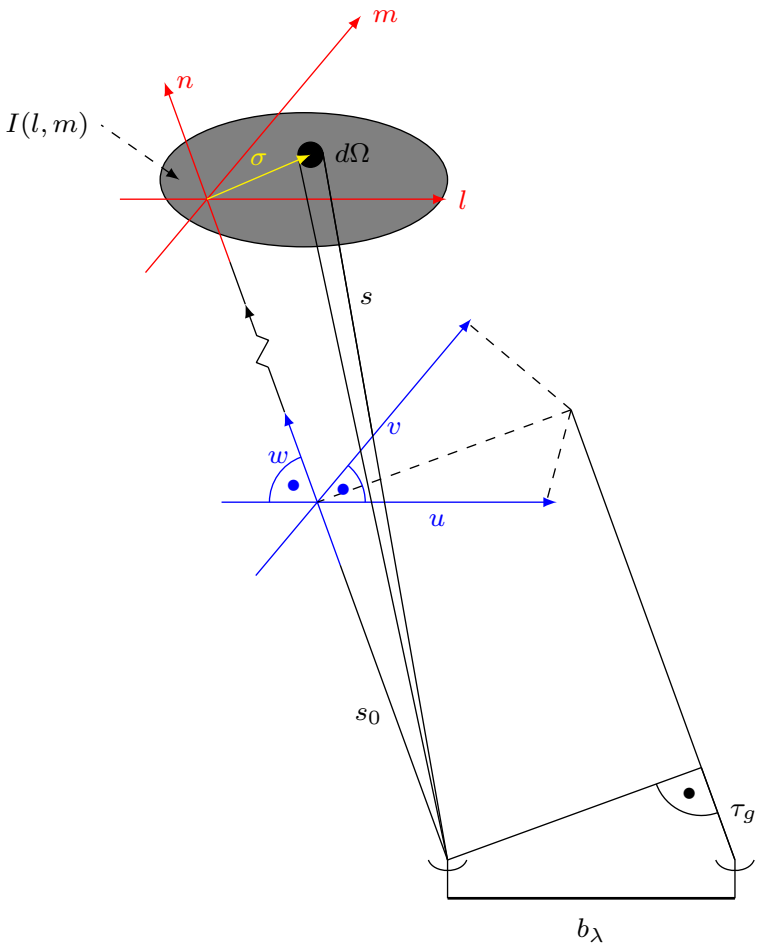

Figure 1.12.: Concept of the used coordinate systems. Taken from: Burd (2017).

By absorbing the exponential factor, the spacial coherence function relative to the phase tracking center $\vec{s}_0$ is independent of w and given by

$$V_\nu(u, v) = \iint I_\nu(l, m) e^{-2\pi i(ul+vm)} \, \mathrm{d}l \, \mathrm{d}m. \tag{1.22}$$

The spatial coherence function is the measured quantity of a radio interferometer. Of interest is the intensity distribution of the source I_ν, which can be obtained with an inverse Fourier transformation. However, two effects need two be considered when handling a measured coherence function. The first effect is based on the fact that a radio interferometer can sample the coherence function only at some points. This leads to gaps in the so-called (u, v)-plane and a loss of Fourier-components in the image. Therefore, the image reconstruction is not trivial and explained in Section 2.1. This can be accounted for by a sampling function $S(u, v)$ in the form

of $S(u,v) = \sum_k w_k \, \delta(u - u_k)\delta(v - v_k)$, which only has non-zero values, where the (u,v)-plane is filled.

Therefore, the inverse Fourier transform of Equation 1.22 is not the true intensity distribution, but a so called dirty image

$$I_\nu^D(l,m) = \iint V_\nu(u,v) S(u,v) e^{2\pi i(ul+vm)} \, \mathrm{d}u \, \mathrm{d}v, \tag{1.23}$$

which is a convolution of the intensity distribution with the so called dirty beam

$$B^D(l,m) = \iint S(u,v) e^{-2\pi i(ul+vm)} \, \mathrm{d}u \, \mathrm{d}v. \tag{1.24}$$

The second effect accounts for the reception pattern of the radio antenna described by the primary beam B^P given by

$$B^P(u,v) = \iint A_\nu(l,m) e^{-2\pi i(ul+vm)} \, \mathrm{d}l \, \mathrm{d}m, \tag{1.25}$$

in which $A_\nu(l,m)$ describes the sensitivity of the antenna. The complex visibility function $V(u,v)$ is then the convolution of the primary beam and the spacial coherence

$$\boldsymbol{V(u,v) = \iint A_\nu(l,m) I_\nu(l,m) e^{-2\pi i(ul+vm)} \, \mathrm{d}l \, \mathrm{d}m.} \tag{1.26}$$

The reconstruction of the true brightness distribution out of the dirty image is explained in the next chapter.

1.2.1. MOJAVE

Monitoring Of Jets in Active galactic nuclei with VLBA Experiments (MOJAVE) is a long-term monitoring program of AGN, specifically their jets, the evolution of their jets, and their polarization properties. Starting in 1994 with 132 sources (Kellermann et al. 1998), today more than 300 objects categorized in several different catalogs have been observed. MOJAVE uses the Very Long Baseline Array (VLBA), a VLBI network spread across North-America consisting of ten identical 25-meter radio telescopes. A map with all stations is shown in Figure 1.13. With the longest baseline stretching 8611 kilometers from Mauna Kea, Hawaii to St. Croix, U.S. Virgin Islands, the VLBA reaches a very high resolution, as shown in the previous section. Observations can be made between 0.3 GHz and 96 GHz divided into several

Figure 1.13.: The VLBA array on the northern hemisphere. Credit: NASA's Goddard Space Flight Center.

discrete bands.

1.2.2. TANAMI

With the Fermi Space Telescope launch, the VLBA became an essential instrument for monitoring newly discovered γ-bright AGN. However, only capable of observing sources up to a declination of -30°, a large area with potentially new γ-observed AGN is not in reach for the VLBA. This lead to the development of the Tracking Active Galactic Nuclei with Austral. Milliarcsecond Interferometry (TANAMI) program, presented in Ojha et al. (2010). It uses the Long Baseline Array (LBA) antennas spread across Australia and other antennas in Australia, South Africa, Antarctica, and South America. A map with TANAMI stations is shown in Figure 1.14. Observations are done at 8.4 GHz and 22 GHz. Initially starting with a sample of 43 sources (Ojha et al. 2010), TANAMI is today not only monitoring a great variety of AGN but also plays a crucial role in multiwavelength studies with other experiments like Fermi, Swift, or XXM-Newton.

Figure 1.14.: The TANAMI array on the southern hemisphere. Credit M. Kadler & J. Wilms.

2. Methods

2.1. Image Synthesis in DIFMAP

In this thesis, the program DIFMAP developed by Shepherd (1997) is used to obtain the images from all VLBA and TANAMI observations of the blazars. All data already went through a phase and amplitude calibration process (see Greisen (2003) for more information about the calibration process).

The imaging process described in this section follows a procedure based on Shepherd (1997) and the DIFMAP-cookbook[1].

As described in the previous section, the measured visibility is the Fourier transform of the source brightness distribution. However, with the inverse Fourier transform, not the true brightness distribution is obtained but the dirty image, which is the convolution of the true brightness distribution with the dirty beam. The dirty beam is the Fourier transform of the sampling function and can be adjusted with a weighting function for the data points (Thompson et al. 2017). In *natural weighting*, all data points get the same weighting factors, which is done if the averaging time is the same for all data points. In *uniform weighting*, the data points are weighted with a factor inversely proportional to the number of data points in the (u, v)-plane. Natural weighting usually leads to a better signal-to-noise ratio, while uniform weighting results in higher resolutions.

The first step in the imaging process is to edit the data by finding and removing (flagging) bad data in the visibilities. This is done in a visual-judgment way, in which data points are removed if they do not fit the rest of the data well. This is the case if the value of the datapoint itself is too high or too low or if the data's error bar is magnitudes higher than the rest of the data. The user has to find a balance between removing too little data, which results in bad data in the model and removing too much data, which reduces the observation's significance and is a waste of observation time.

[1] ftp://ftp.astro.caltech.edu/pub/difmap/difmap.html

After visiting and flagging the data, the so-called difference mapping can be started. It uses a combination of the `clean` algorithm developed by Högbom (1974) and self-calibration to approximate the actual brightness distribution in an iterative process called hybrid imaging (Pearson and Readhead 1984). Both techniques will be explained here.

The `clean` algorithm works in an iterative way:

1. A rectangle is selected in the dirty map, called `clean` window, where `clean` finds the point of highest intensity.
2. The peak intensity is multiplied with the dirty beam and a loop gain and subtracted from the dirty map.
3. The position and amplitude of this point are added to the `clean` model via a δ-function.
4. Repeat steps 1 to 3 until no significant emission is left to clean.
5. Select a second `clean` window and repeat all steps until there is no significant emission left in the residual map.

The clean image is then derived by convolving the `clean` model with all δ functions with a clean beam, usually a Gaussian, where the full width at half maximum (FWHM) is equal to the dirty beam.

Although the data went already through a calibration process, it is likely that there are still residual errors in the phase and amplitude data. In `DIFMAP`, this can be solved with self-calibration. The closure phase is the sum of the visibility phases of three baselines connected in a closed-loop. A similar concept exists for the closure amplitude, which is based on four antennas. Self-calibration uses the fact that antenna-based errors cancel out for these closure quantities. See Jennison (1958) or Cornwell and Fomalont (1999) for more detailed information.

To determine the noise level and thereby the 3-σ confidence level in each image, two assumptions are made: The source is only located in the center and does not stretch to the borders of the image. And other than the observed source, the image is only filled with uniform noise. With these assumptions, the noise level outside a square in the middle of the image covering ~50% of the total field is determined and set to the image's total noise level. This method is also done with all polarization images, stacked total intensity images, and stacked polarization images.

2.1.1. Ambiguity of Imaging

In this section, the ambiguity of the imaging process of VLBI observations is shown on the example of PKS 1502-106. The observation of this source obtained on 30 August 2019 with the VLBA contains data in the U, K, and Q-band, corresponding to 15 GHz, 24 GHz, and 43 GHz. In a first approach, each dataset was imaged separately with no respect to the others with uniform and natural weighting. In Figure 2.1 the images at 24 GHz in uniform and 43 GHz in natural weighting are shown. The first shows a distinctive narrowing of the jet and a following expansion, creating a wing-like structure. The second image also shows a narrowing and a following expansion of the jet but lacks the out-most tips of the wing structure.

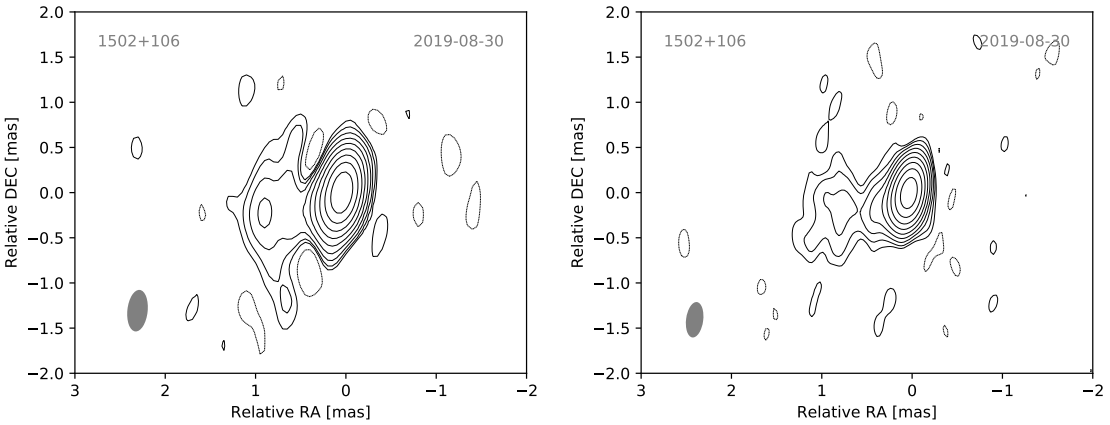

Figure 2.1.: Left: 24 GHz image of PKS 15502-106 in uniform weighting observed at 28 February 2013 with the VLBA. The lowest contour line is 0.21% of the map peak of 1.59 Jy/beam. Right: 43 GHz image in natural weighting of the same observation. The lowest contour line is 0.24% of the map peak of 0.577 Jy/beam.

Assuming this is a valid representation of this source, one can estimate an upper limit of the spectral index at the tip of the wings by taking the lowest contour line of the 43 GHz image as an upper limit for the flux density at this point and the second contour line in the 24 GHz image. The spectral index α is then calculated with

$$\alpha = \frac{log(S_2/S_1)}{log(\nu_2/\nu_1)}, \tag{2.1}$$

which leads to an upper limit of $\alpha_{24\,\mathrm{GHz}-43\,\mathrm{GHz}} < -2.55$. Since this value is beyond all expectations for a source of this type, there are two possible explanations: The wing structure is real and was lost in the imaging process of the 43 GHz observation, or it is not real and was artificially created in the imaging of the 24 GHz observation.

To check both hypotheses, the 24 GHz data was imaged a second time but with the `clean` windows of the 43 GHz observation and vice versa, both shown in Figure 2.2. While the image at 43 GHz does not change substantially, the wing structure in the 24 GHz image is nearly completely gone, and the source shows a morphology similar to the other image. At the same time, the noise level is increased by only 33%. This leads to the conclusion that the wing structure in the 24 GHz image is most likely an artifact and has no real counterpart.

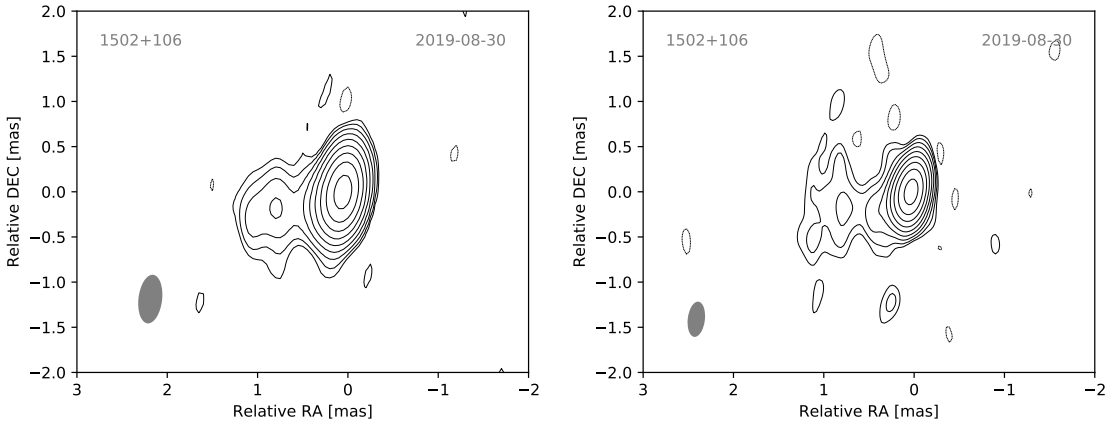

Figure 2.2.: Left: 24 GHz image of PKS 15502-106 in uniform weighting imaged with the `clean` windows of the 43 GHz map in Figure 2.1. The lowest contour line is 0.28% of the map peak of 1.62 Jy/beam. Right: 43 GHz image in natural weighting with the `clean` windows of the 23 GHz image in Figure 2.1. The lowest contour line is 0.26% of the map peak of 0.581 Jy/beam.

This example shows that the imaging process of VLBI data, here performed with `DIFMAP` and its `clean` algorithm, is not unambiguous. One has to be careful with the interpretation of such data. If possible, the comparison to other images of the source, i.e., at other wavelengths, can support the imaging process and reveal nonphysical features and image artifacts.

2.1.2. Image Artifacts

Figure 2.3 left shows a first imaging approach of the 15 GHz data in natural weighting of PKS 1502+106 from the observation obtained on 28 February 2013 with the VLBA.

A noisy band that stretches across the source in a north-south direction is visible. The phase and amplitude data for each baseline were investigated to find the origin of this noise pattern. A typical, properly imaged baseline is shown in the left of

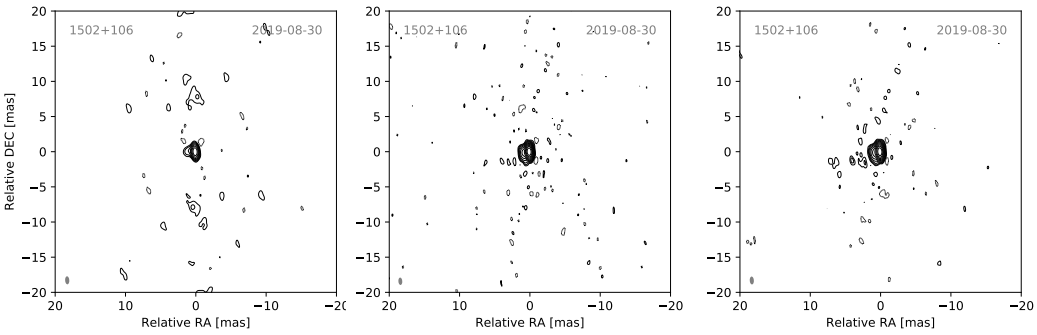

Figure 2.3.: Left: First imaging approach of 15 GHz data in natural weighting of PKS 1502+106 observed at 28 February 2013 with the VLBA. The lowest contour line is 0.80% of the map peak of 2.21 Jy/beam. A noisy band stretches across the image in a north-south direction. Middle: Same data and imaging process but without the data from the station Pie Town. The lowest contour line is 0.10% of the map peak of 2.30 Jy/beam. The noisy band is less prominent, and the noise level is reduced to one-eighth. Right: Same data and imaging process but with the re-included data from the station Pie Town. The lowest contour line is 0.10% of the map peak of 2.26 Jy/beam.

Figure 2.4, where the amplitude over time is plotted on the top and the phase over time is plotted on the bottom, each in pink. The current model is shown in red. The same is shown in Figure 2.4 in the right for a baseline with the station Pie Town. Here, the red model represents the amplitude values much worse than in Figure 2.4 on the top.

This behavior is visible for all baselines of Pie Town, which indicates that this station does not fit well with the model. To compensate for this, the data was imaged again but without the data from Pie Town. The result of this imaging process is shown in Figure 2.3 middle. The noisy band stretching from north to south across the source is less prominent, and the noise in the image is more uniform than in Figure 2.3. Also, the 3-σ level is decreased to one-eighth. However, in this version, Pie Town's data is lost, although it is, in general, not bad.

The current model was frozen, and the re-included Pie Town data with the `DIFMAP` command `selfcal` fitted to the model. The result with the re-included Pie Town data is shown in Figure 2.3 right. The 3-σ noise level is the same as before, and the overall noise pattern in the image is relatively uniform. The 15 GHz data in uniform weighting shows the same behavior.

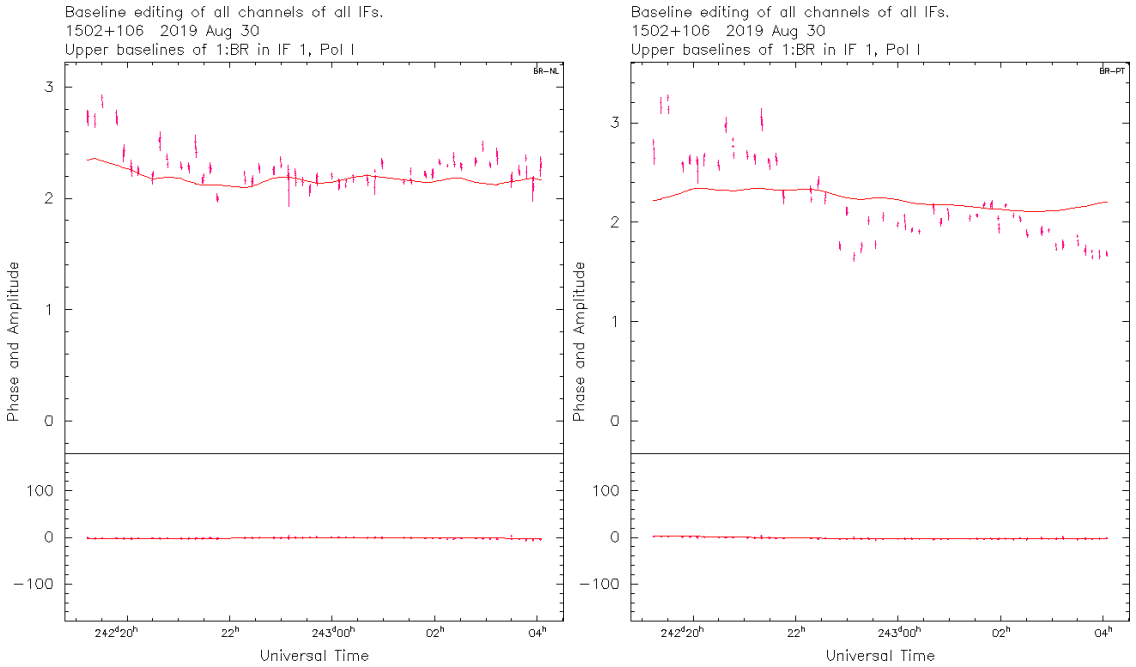

Figure 2.4.: Left: Example of a proper imaged VLBI baseline. The data is shown in pink, the model in red. Right: A baseline including Pie Town. The model represents the shown data worse than in the left image.

2.2. Polarization Images

Not only the total intensity images but also the polarized images presented in this thesis are produced in `DIFMAP` with the `clean` algorithm. This was done by imaging the channels Stokes U and Q after imaging the total intensity image. The process is based on the assumption that a given point in the image can only show polarized flux if a significant flux is visible in the total intensity image. Therefore, after imaging the latter, `clean` windows were set in all relevant areas, all areas inside the 3-σ level that belong to the core and the jet of the source shown in Figure 2.5.

After selecting U and Q, a large number of `clean` and self-calibration cycles were applied so that another iteration would not change much of the model. This procedure was then done with both channels. The polarization P and its corresponding Electric-Vector-Position-Angle $EVPA$ are then calculated pixelwise with the U and Q-images according to Lister and Homan (2005) with

$$P = \sqrt{U^2 + Q^2} \quad \text{and} \quad EVPA = \frac{1}{2}\, arctan\left(\frac{U}{Q}\right). \tag{2.2}$$

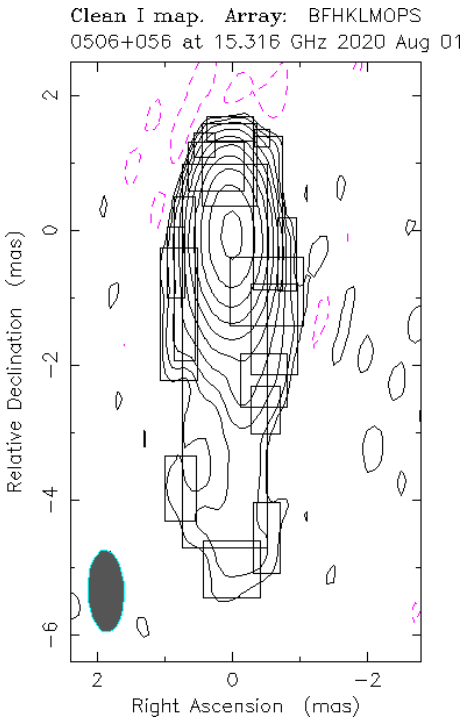

Figure 2.5.: `clean` windows applied on a cleaned total intensity image for producing U and Q-images to calculate the polarization images.

2.3. Stacking Methods

A central part of this thesis was producing stacked images of VLBI observations. This was done with total intensity images and polarization images. While the stacking of total intensity images is reasonably straightforward, the stacking of polarized images can be done with two different methods, as shown below. For previous approaches of stacking see Lister et al. (2009) or Walker et al. (2018). An example of how a stack of polarized VLBI images reviles new information is shown in Beuchert et al. (2018).

2.3.1. Total Intensity Image

The stacking of the total intensity images is done in a straightforward way. All epochs are stacked pixel-wise, where the value of an individual pixel z_{stack} is calculated to

$$z_{\text{stack}} = \frac{1}{n} \sum_{i=1}^{n} z_i, \tag{2.3}$$

in which z_i is the pixel value of epoch i and n is the total number of epochs.

Ideally, all stacked epochs have the same beam. In this thesis, however, also epochs with different beams are stacked (see Chapter 3). This was only done with images from the VLBA because their beams are similar in size and orientation. Therefore, the stack of these images is similar to a stack of images with the same beam.

2.3.2. Polarized Intensity Image

After imaging U and Q of multiple epochs, two different approaches to a stacked polarized image are explored. The two methods are summarized in Figure 2.6 and will be explained in detail below.

Method 1

In the first method, U and Q are stacked pixelwise:

$$Q_{\text{stack}} = \frac{1}{n} \sum_{i=1}^{n} Q_i \text{ and } U_{\text{stack}} = \frac{1}{n} \sum_{i=1}^{n} U_i. \tag{2.4}$$

With the stacked U and Q channels, P_{stack} and $EVPA_{\text{stack}}$ are calculated according to Equation 2.2

$$P_{\text{stack}} = \sqrt{U_{\text{stack}}^2 + Q_{\text{stack}}^2} \quad \text{and} \quad EVPA_{\text{stack}} = \frac{1}{2} \, arctan\left(\frac{U_{\text{stack}}}{Q_{\text{stack}}}\right). \tag{2.5}$$

Since U and Q have positive and negative values, in this method, the values from a given pixel can cancel each other out. Therefore, regions with alternating values between different images can appear as if there is no polarization.

Method 2

The second method first calculates P_i and $EVPA_i$ for each epoch i:

$$P_i = \sqrt{U_i^2 + Q_i^2} \quad \text{and} \quad EVPA_i = \frac{1}{2} \, arctan\left(\frac{U_i}{Q_i}\right), \tag{2.6}$$

and then stacks P_i and $EVPA_i$ pixelwise:

$$P_{\text{stack}} = \frac{1}{n} \sum_{i=1}^{n} P_i \quad \text{and} \quad EVPA_{\text{stack}} = \frac{1}{n} \sum_{i=1}^{n} EVPA_i. \tag{2.7}$$

A variation of this method is to calculate $EVPA_{\text{stack}}$ with a weighted sum, in which P_i are the weights:

$$EVPA_{\text{stack}} = \frac{\sum_{i=1}^{n} P_i \, EVPA_i}{\sum_{i=1}^{n} P_i}. \tag{2.8}$$

Compared to the first method, U and Q values from different epochs can not cancel each other out. Since this method represents how much a given point in the stacked image was polarized in all stacked epochs, the polarization and EVPAs are shown for all regions of interest. Here, all regions within the first contour corresponding to a 3-σ noise level in the stacked total intensity image are shown.

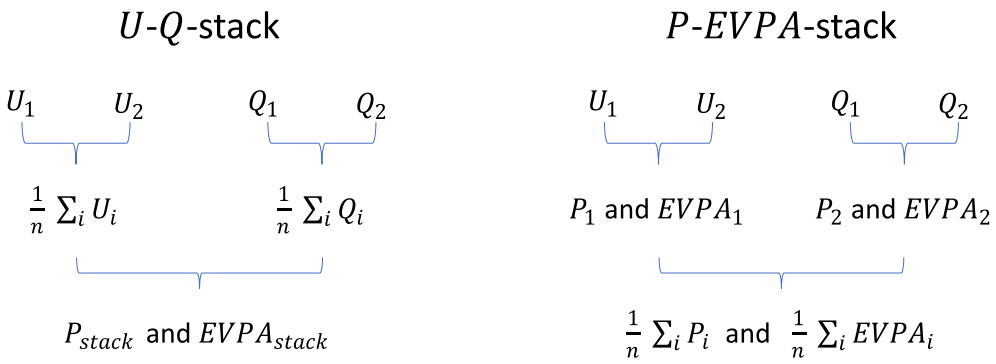

Figure 2.6.: The two different stacking methods for polarized images in comparison.

2.4. Spectral Index Images

In this thesis, a VLBA observation of PKS 1502+106 with 15 GHz, 24 GHz, and 43 GHz data obtained on 8 August 2019 was imaged. With images at different wavelengths, it is possible to generate spectral index maps. For combining two images to a spectral index map, particular preparations need to be done to those images:

First, both need to be convolved with the same beam. In this thesis, this was done in `DIFMAP` with a combination of `taper` and `restore`. A (u, v)-taper weights down individual visibilities with two values to set: The (u, v)-radius defines which visibilities with a greater (u, v)-radius than the defined value will be weighted down. Furthermore, the Gaussian taper value defines the percentage to which the visibilities will be weighted down. A tapered image loses angular resolution compared to a non-tapered image. However, it is easier to find possible extended structures in

the image. `taper` was used to get the beams to a similar size. `restore` convolves then the image with a chosen beam. Combining both methods is necessary because brute-forcing a much larger beam to data can lead to image artifacts.

Second, the images need to be aligned because applying self-calibration loses the absolute position on the sky. Here, the images were aligned so that both images' map peaks lie on top of each other.

The spectral index maps in this thesis are calculated in a pixel-wise manner. If the two images differ in resolution, the smaller image is upscaled to avoid aliasing artifacts when downscaling an image. This was done with the `skimage.transform.resize` function provided in the `scikit-image` packege for Python 3 (see Walt et al. 2014).

The individual pixels α_i of the spectral index map are then calculated with

$$\alpha_i = \frac{\log\left[z_i(\nu_2)/z_i(\nu_1)\right]}{\log\left[\nu_2/\nu_1\right]} \tag{2.9}$$

in which z_i are the pixels of the two images at frequency ν_1 and ν_2 with $\nu_1 < \nu_2$.

This was done with every pixel that exceeded in both images the 3σ threshold, so only areas are plotted in the spectral index map that lie inside the first contour line in both images.

3. Results

This chapter presents imaging results of the three observed blazars, PKS B1424-418, TXS 0506+056, and PKS 1502+106. All images are obtained in DIFMAP and unless otherwise stated, the lowest contour line is set to a 3σ-noise level.

3.1. PKS B1424-418

For PKS B1424-418, ten epochs obtained with TANAMI were imaged, ranging from 11 November 2007 to 14 March 2013. After a first approach to imaging the data, it became clear that the source shows emission up to a distance of tens of mas from the core. To get a better understanding of the source's morphology, all epochs were imaged with a (u, v)-taper.

3.1.1. Tapered Images

Figure 3.1 shows two exemplary images of PKS B1424-418. All ten images can be found in Appendix A, Figure A.1. The corresponding image properties are listed in Table A.1. In all images, a Gaussian taper was applied, and additionally the clean-map was convoluted with the same beam of $7.6\,\text{mas} \times 7.6\,\text{mas}$ at 0°. The beamsize of $7.6\,\text{mas}$ is 75% of the mean of the major axis of the beams of all observations.

The source reveals a bright core with additional structure towards the north-east in all images. A clear jet is not visible in all epochs. In two images, the ones shown in Figure 3.1, hints of limb brightening are visible at a distance of $\sim 40\,\text{mas}$ from the core.

Figure 3.2 shows the stacked image of the tapered total intensity maps. Again the bright core and a jet in a north-eastern direction are visible, as well as the hints of limb-brightening at a distance of $\sim 40\,\text{mas}$ from the core. The jet also shows a radial structure, specifically a bright feature at a distance of $\sim 30\,\text{mas}$ from the core. This structure is also visible in the single epochs, especially in the later ones, where the jet is not continuous but rather consisting only of this feature.

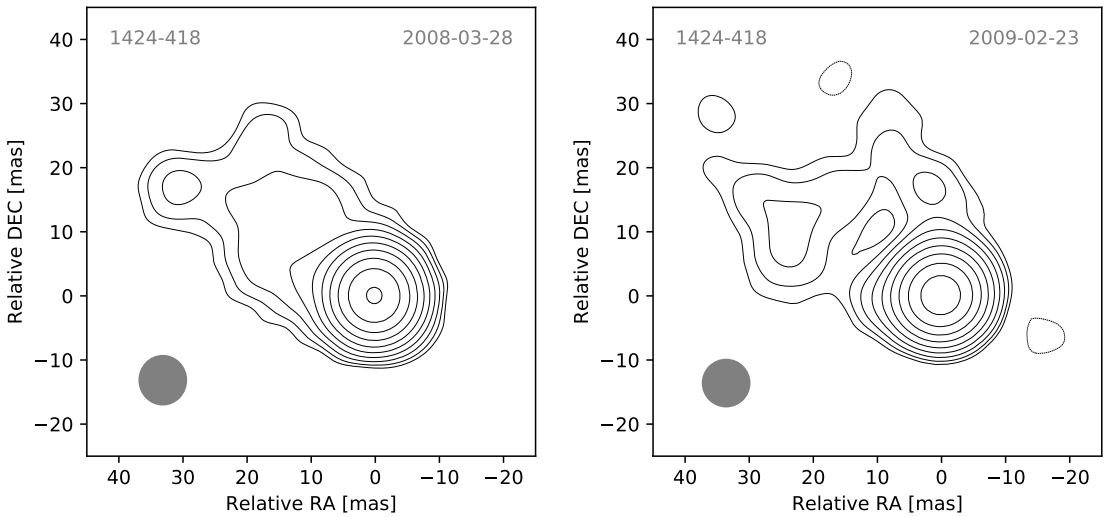

Figure 3.1.: Two exemplary images of PKS B1424-418 that show hints of limb-brightening. Both images are tapered and convoluted with the same beam.

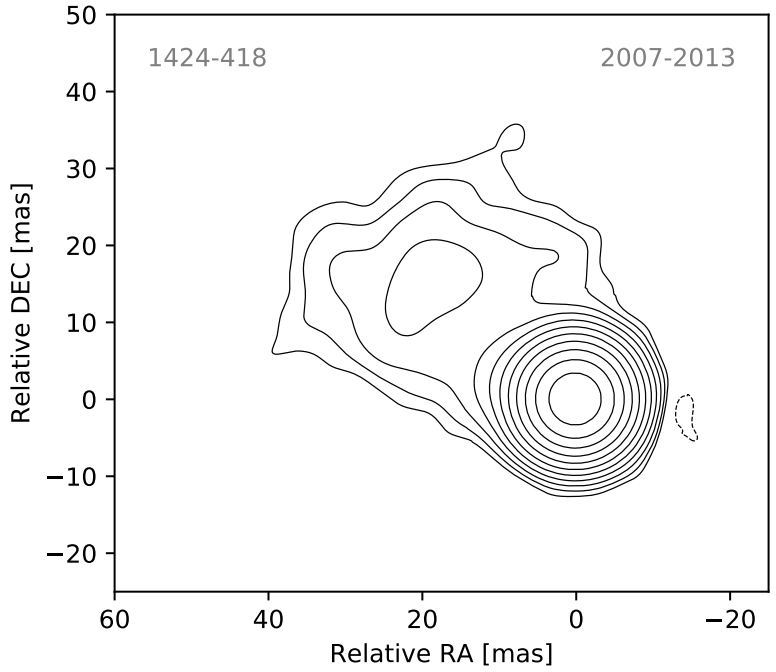

Figure 3.2.: Stacked total intensity image of PKS B1424-418. A total of ten tapered images that were convolved with the same beam went into the stack. S_{peak} = 2.05 Jy beam^{-1}, σ_{rms} = 0.388 mJy beam^{-1}

3.1.2. Full Resolution Images

Figure 3.3 shows the same images of PKS B1424-418 as in Figure 3.1 but without a (u, v)-taper in full resolution. All ten full resolution images can be found in Appendix A, Figure A.2. The corresponding image properties are listed in Table A.2.

The source shows a bright core with a structure extending to the north-east. Compared to the tapered images, this structure is not visible as a continuous jet but as individual features. Because they appear different in every epoch, a stacked image would not reveal any more information and was not done with the full resolution images.

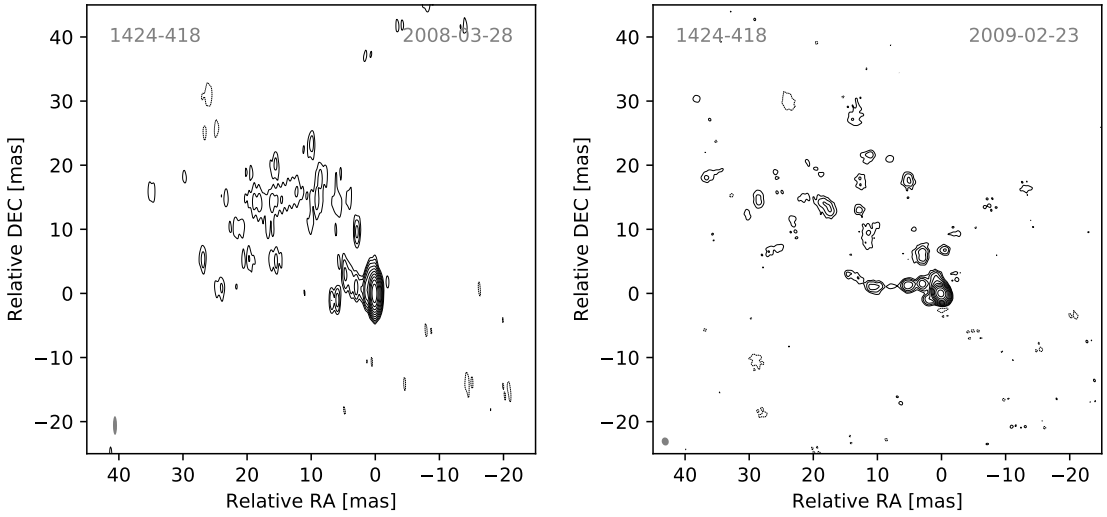

Figure 3.3.: Two exemplary images of PKS B1424-418 in full resolution.

3.2. TXS 0506+056

For TXS 0506+056, all publicly available MOJAVE data accessible on the MOJAVE website[1] was used. There are 24 epochs available from 7 January 2009 to 1 August 2020 with polarization data for all of them. Figure 3.4 shows two exemplary images of TXS 0506+056. All 24 images can be found in Appendix A, Figure A.3 and Figure A.4. The corresponding image properties are listed in Table A.3.

In all images one can see the total intensity in contour lines, the total polarization as a colormap, and the EVPAs as vectors in the image. The lowest contour line for the total intensity, as well as the lowest shown polarization is set to a 3σ-noise level EVPAs are only shown where the polarization is above the 3σ threshold.

The source shows a bright core with a jet expanding to the south in all images. The jet shows in several images limb brightening, e.g., the ones shown in Figure 3.4. All epochs show polarization in the core and, to some degree, also in the jet. The core always has the brightest polarization. In some epochs, a bright polarized feature south (e.g., 3 June 2009), south-west (e.g., 17 June 2017), or south-east (e.g., 8 May 2020) of the core is visible. EVPAs in the core follow no particular pattern, and the jet polarization is often weak. Therefore no EVPAs are shown.

All 24 images are stacked to produce a stacked total intensity image, shown in Figure 3.5. As described in Section 2.3, ideally, all stacked images have the same beam. However, all of the stacked images of TXS 0506+056 are obtained with the VLBA. This instrument usually operates in the same configuration, which leads to a similar beam in all epochs. This can be seen in Appendix A, Figure A.3 and Figure A.4, where the beams are shown for all images.

In Figure 3.5 on the left, a prominent pattern of image artifacts is seen, stretching from north to south across the source. In the right image, a higher value for the lowest contour line was chosen, corresponding to a 3σ confidence level. A zoomed-in version of the core and the jet is shown in Figure 3.6. The bright core and the jet expanding south are visible, as well as the jet's limb brightening at a distance of $\sim 5\,\mathrm{mas}$ from the core.

As described in Section 2.3, two different methods of stacking multiple polarization images are explored. Figure 3.7 shows the stacked image, where the first method (U-Q-stack) was used. Polarized flux is shown, where it exceeds a 3σ-noise threshold. The core shows the most polarized flux, and compared to the individual epochs, the jet is also clearly visible. EVPAs seem to follow a trend, where they are more

[1] https://www.physics.purdue.edu/MOJAVE/sourcepages/0506+056.shtml

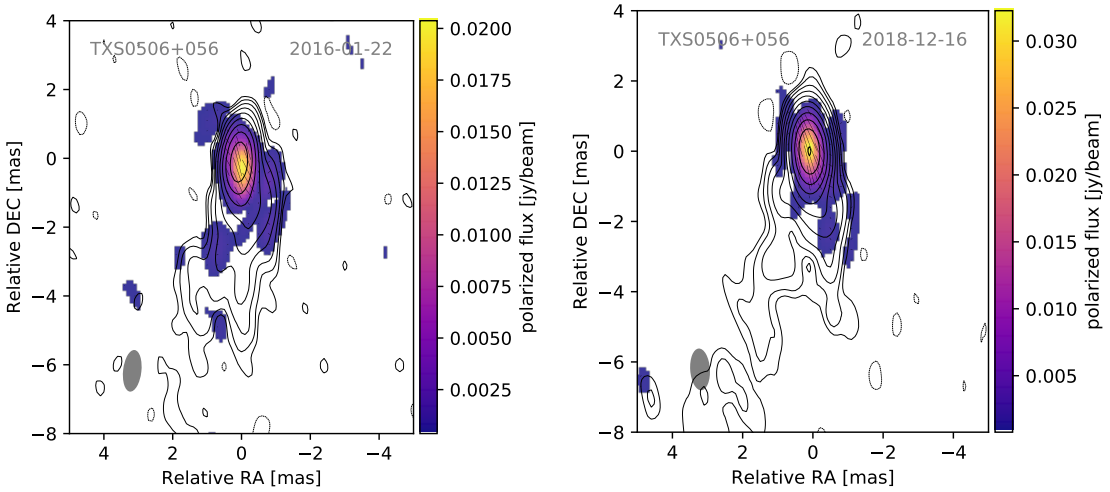

Figure 3.4.: Two exemplary images of TXS 0506-056 that show limb brightening.

parallel to the jet at the core and in the inner parts of the jet and orthogonal in the outer parts. This behavior can be seen on the western side of the jet and especially on the eastern side.

In contrast, the stacked polarized image obtained with the second method (P-EVPA-stack) is shown in Figure 3.8. Here, polarized flux is shown inside the first contour line of the total intensity stack to highlight how much a given point in the jet was polarized over time. EVPAs in the image show that this is a reasonable approach: For random noise, EVPAs are expected to be oriented randomly. However, this is not the case. On top of that, the outer parts of the jet show EVPAs that follow the trends of their neighbors.

The stacked polarized image is similar to the first method, shown in Figure 3.7. The core shows the most polarized flux. Inside the jet, only little variation of the polarized flux is seen. EVPAs seem to follow the same trend as in the first method; however, the trend of parallel EVPAs in the middle of the jet and orthogonal EVPAs in the outer regions is not so clear. Especially the outer parts also show EVPAs parallel to the jet.

Figure 3.9 was also obtained using the second method. However, the EVPAs are weighted with the polarized flux as their weights in the stacked image. The overall appearance is very similar to the image where the EVPAs are not weighted. However, the trend of EVPAs orthogonal to the jet in the jet's outer layers is stronger than in Figure 3.8 and similar to the first method in Figure 3.7.

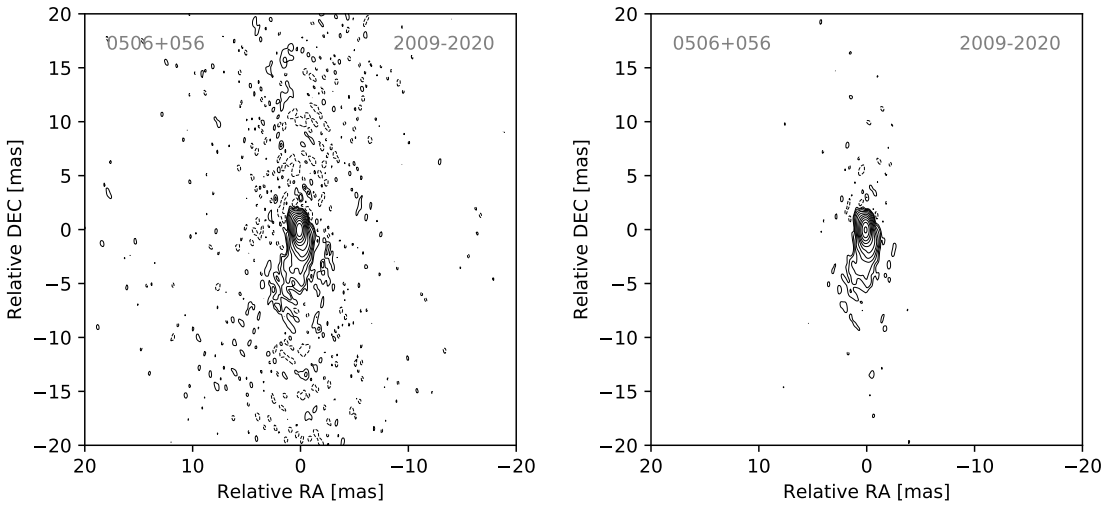

Figure 3.5.: Stacked total intensity image of TXS 0506+056. A total of 24 images went into the stack. The left image illustrates artefacts north and south of the source. The right image is plotted with a 3-σ lowest contour line.

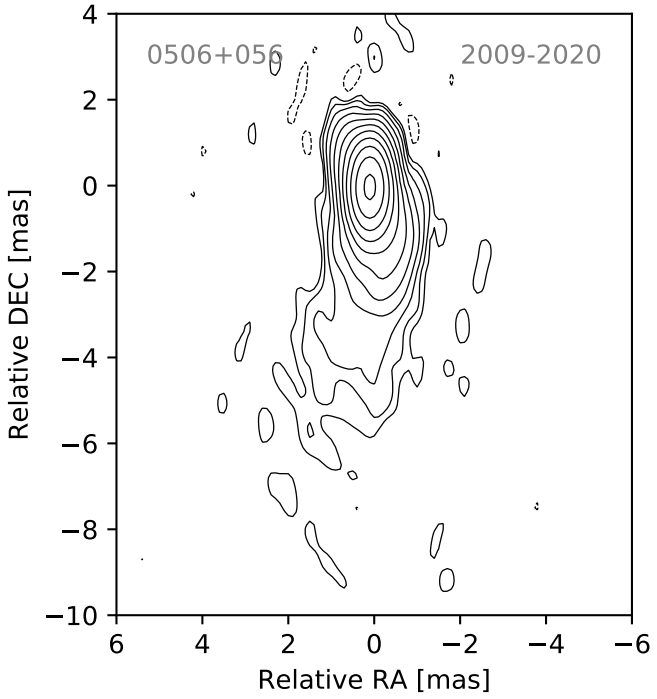

Figure 3.6.: Zoomed-in version of the total intensity stack of TXS 0506+056. S_{peak} = 0.742 Jy beam^{-1}, σ_{rms} = 0.208 mJy beam^{-1}.

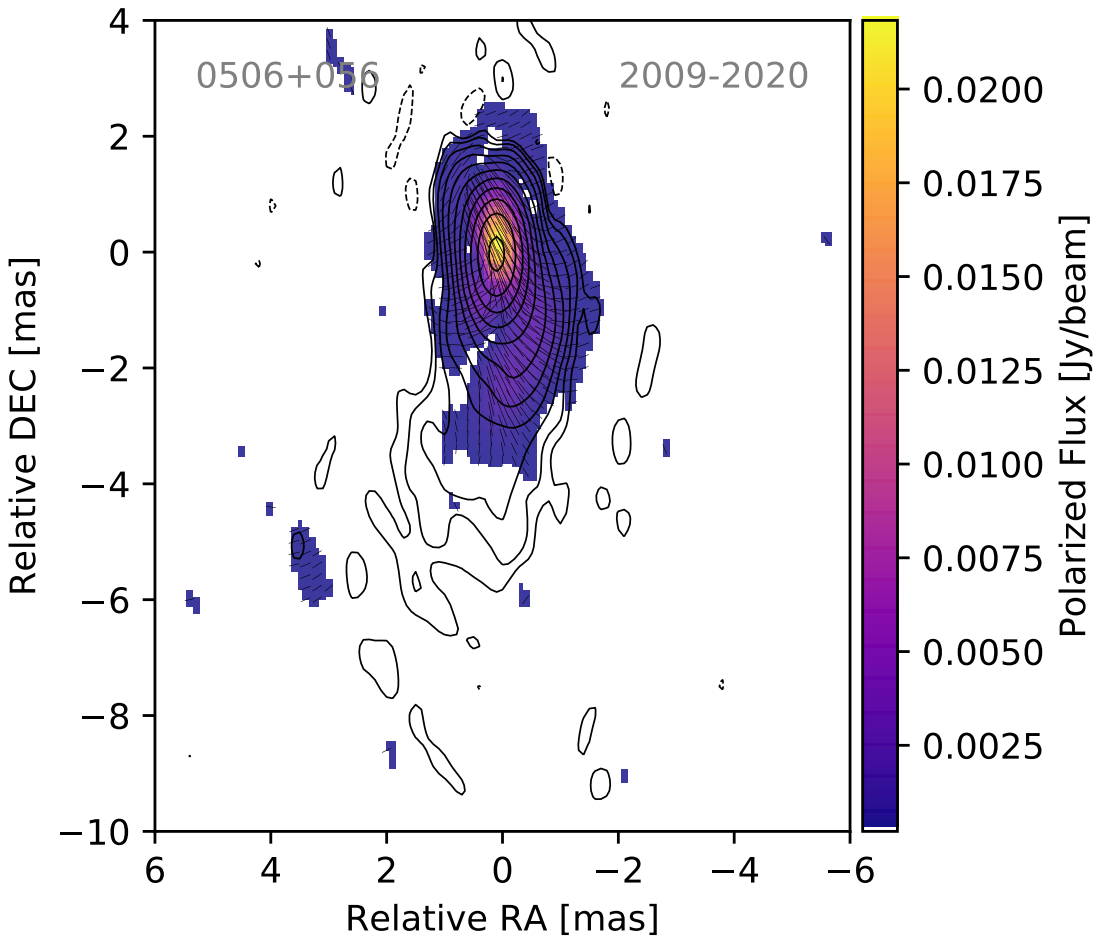

Figure 3.7.: Stacked total intensity image of TXS 0506+056 shown in contour lines overlayed with the stacked polarized image shown in color, together with the EVPAs. The stacked polarized image was produced with the 'U-Q-stack'-method as described in Section 2.3.

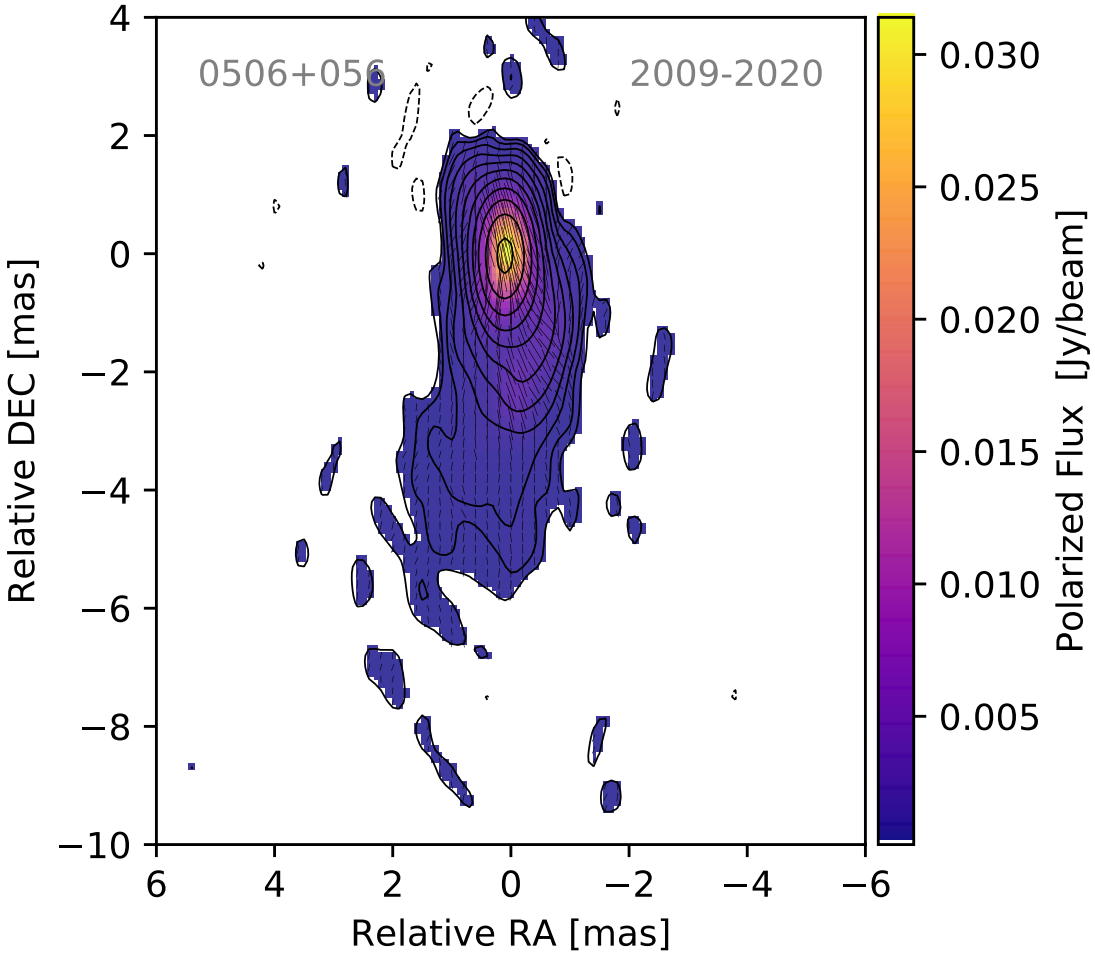

Figure 3.8.: Stacked total intensity image of TXS 0506+056 shown in contour lines overlayed with the stacked polarized image shown in color, together with the EVPAs. The stacked polarized image was produced with the 'P-EVPA-stack'-method as described in Section 2.3.

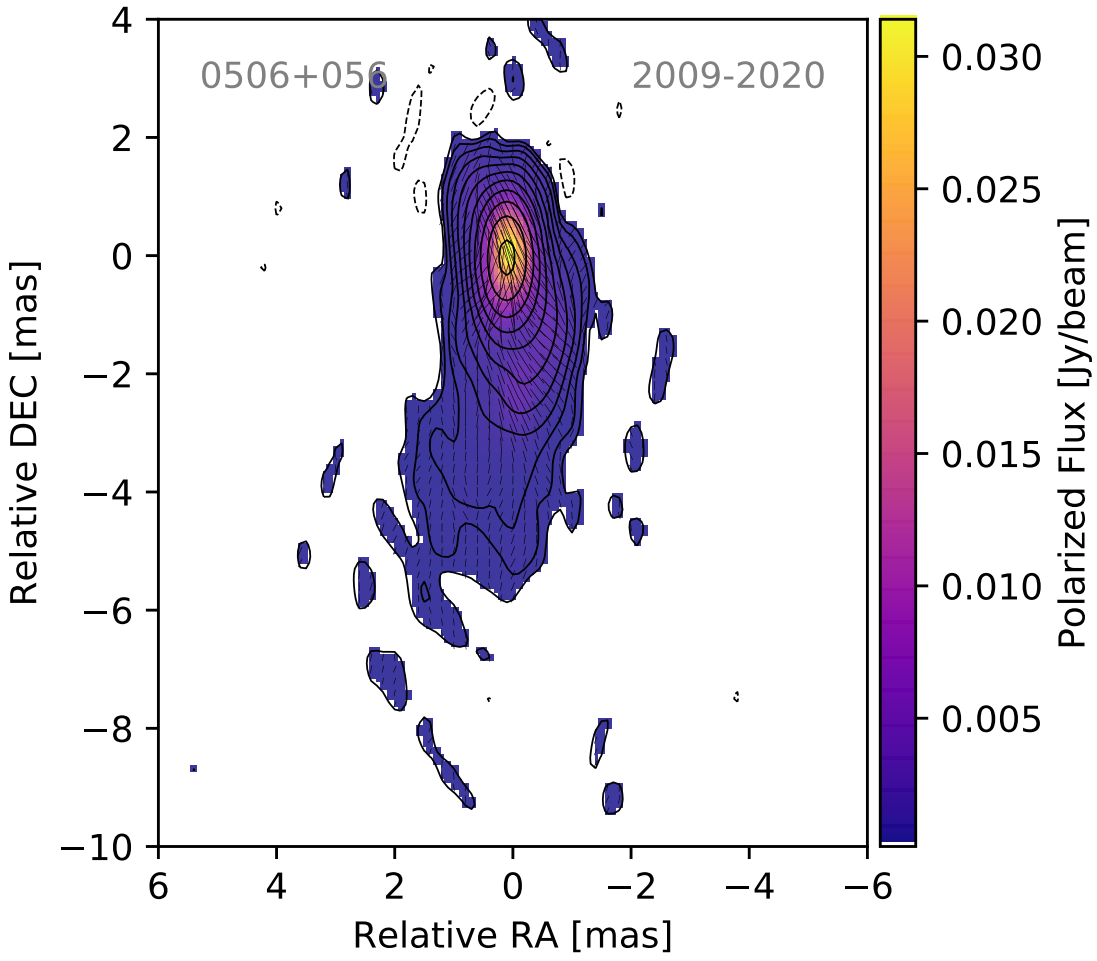

Figure 3.9.: Stacked total intensity image of TXS 0506+056 shown in contour lines overlayed with the stacked polarized image shown in color, together with the EVPAs. The stacked polarized image was produced with the 'P-EVPA-stack'-method as described in Section 2.3. Different to Figure 3.8, EVPAs are weighted with the polarized flux as their weights.

3.3. PKS 1502+106

For PKS 1502+106, also all publicly available MOJAVE data accessible on the MOJAVE website[2] was used. There are 28 epochs from 29 March 2003 to 21 October 2020 available that contain polarization information. Note the time gap of eight years between 2011 and 2019, where PKS 1502+106 was not part of the MOJAVE monitoring program. Figure 3.10 shows two exemplary images of the source. All 28 images can be found in Appendix A, Figure A.5 and Figure A.6. The corresponding image properties are listed in Table A.4. One can see the total intensity in contour lines, the total polarization as a colormap, and the EVPAs as vectors in the image.

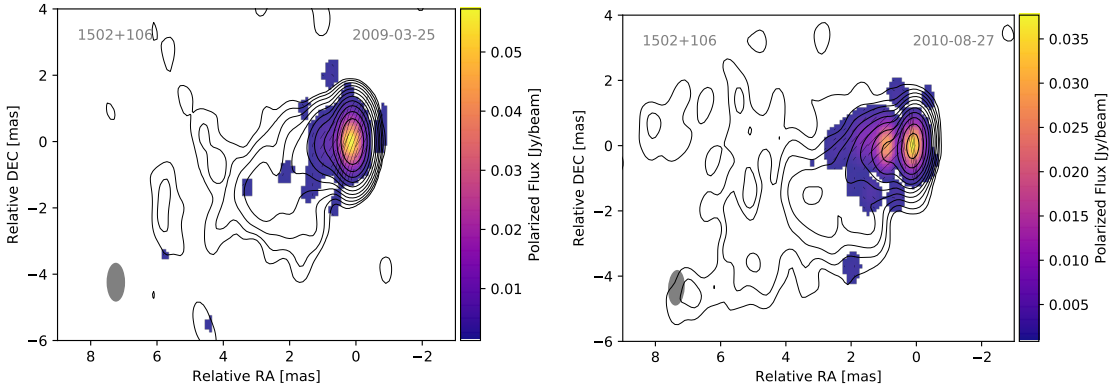

Figure 3.10.: Two exemplary images of PKS 1502+106 that show hints of limb-brightening.

In all images the source shows a bright core with a jet expanding east-south-east. In the later images, the jet is fainter, and in some epochs, barely visible. In some images the jet shows hints of limb brightening, e.g., the ones shown in Figure 3.10. However, this is not as clear as in the case of TXS 0506+056. All epochs show polarization in the core and, to some degree, also in the jet, which is, however, very minimal in some images (e.g., 27 August 2019). The core always shows bright polarization. The image of 18 October 2004 also shows a bright polarized feature south-east of the core. A second bright feature can be seen in the epochs around 25 June 2008 and 19 June 2010, but east of the core. EVPAs in the core follow no particular pattern, and the polarization of the jet is often weak, and therefore no EVPAs are shown.

Again, all 28 images with different beams are stacked to a stacked total intensity image, shown in Figure 3.11. On the left, the similar image artifacts as in the

[2]https://www.physics.purdue.edu/MOJAVE/sourcepages/1502+106.shtml

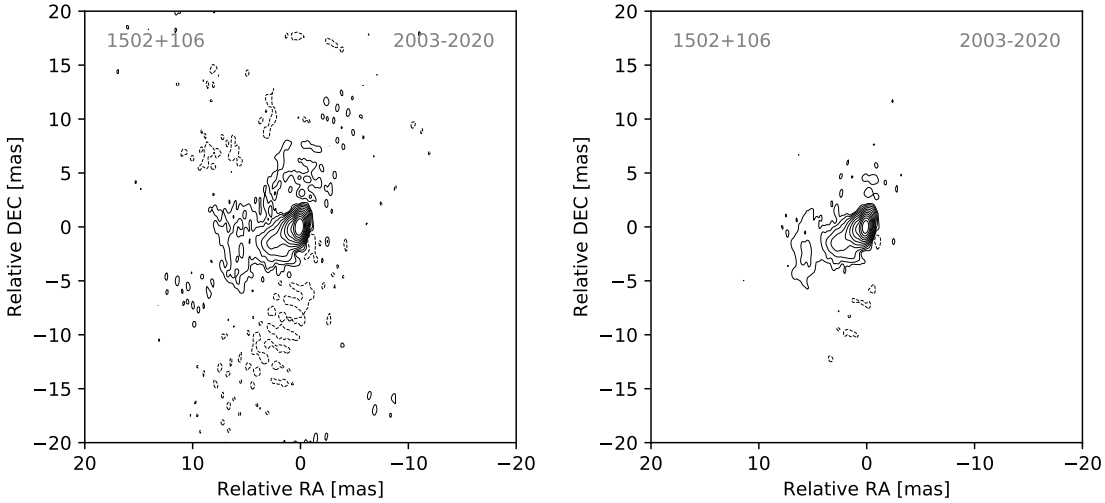

Figure 3.11.: Stacked total intensity image of PKS 1502+106. A total of 28 images went into the stack. The left image illustrates artefacts north and south of the source. The right image is plotted with a 3-σ lowest contour line.

stacked image of TXS 0506+056 are visible. On the right, a higher value for the lowest contour line was chosen, better corresponding to a 3σ confidence level. A zoomed-in version of the core and the jet is shown in Figure 3.12. The bright core and the jet expanding east-south-east are visible. Limb brightening does not appear in the stacked-image.

Both methods for stacking multiple polarization images are applied. Figure 3.13 shows the stacked image, where the first method (U-Q-stack) was applied. Polarized flux is shown where it exceeds a 3σ-noise threshold. The core shows the most polarized flux and compared to the individual epochs, the jet also shows more polarized emission. Also, the bright feature east of the core is visible, as well as the region south-east of the core. EVPAs show a mixed picture: In the inner part of the jet, close to the core, they are parallel to the jet, then turn more towards an orthogonal orientation, and become again parallel at the feature $\sim 4\,\mathrm{mas}$ from the core. Towards the jet's southern side, they rotate to an orthogonal orientation, while on the northern edge, they stay parallel to the jet.

The stacked polarized image obtained with the second method (P-EVPA-stack) is shown in Figure 3.14. Again, EVPAs in the image reveal that displaying all polarized flux inside the first contour line is a reasonable approach. Outer parts of the jet show EVPAs that follow the trends of their neighbors.

This stacked polarized image differs in some aspects from the first method, shown in Figure 3.13. The core still shows the most polarized flux. However, the bright

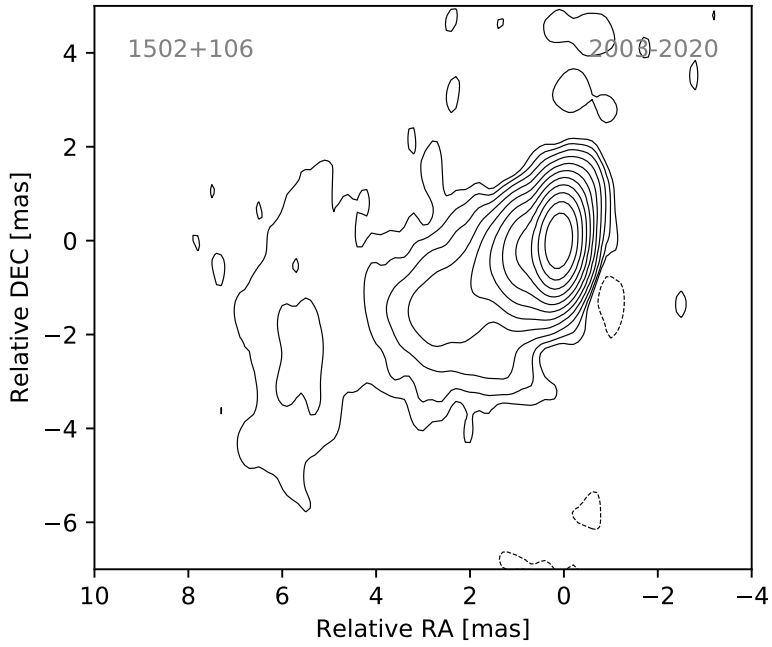

Figure 3.12.: Zoomed-in version of the total intensity stack of PKS 1502+106. S_{peak} = 1.50 Jy beam^{-1}, σ_{rms} = 0.237 mJy beam^{-1}

features east and south-east are very faint, compared to the bright core. EVPAs seem to follow the same trend as in the first method. EVPAs on the northern side of the jet show the trend of being orthogonal to the jet.

Figure 3.15 was also obtained with the second method, but the EVPAs are weighted with the polarized flux as their weights. The overall appearance is very similar to the image in which the EVPAs are not weighted. However, the trend of EVPAs parallel to the jet in the center of the jet is stronger than in Figure 3.14 and similar to the first method in Figure 3.13. EVPAs at the northern edge of the jet show more of a parallel orientation.

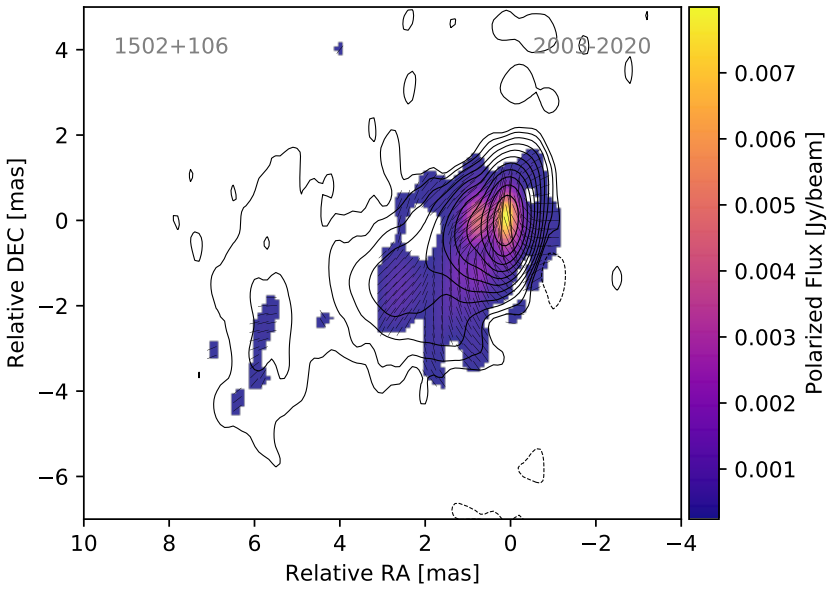

Figure 3.13.: Stacked total intensity image of PKS 1502+106 shown in contour lines overlayed with the stacked polarized image shown in color, together with the EVPAs. The stacked polarized image was produced with the 'U-Q-stack'-method as described in Section 2.3.

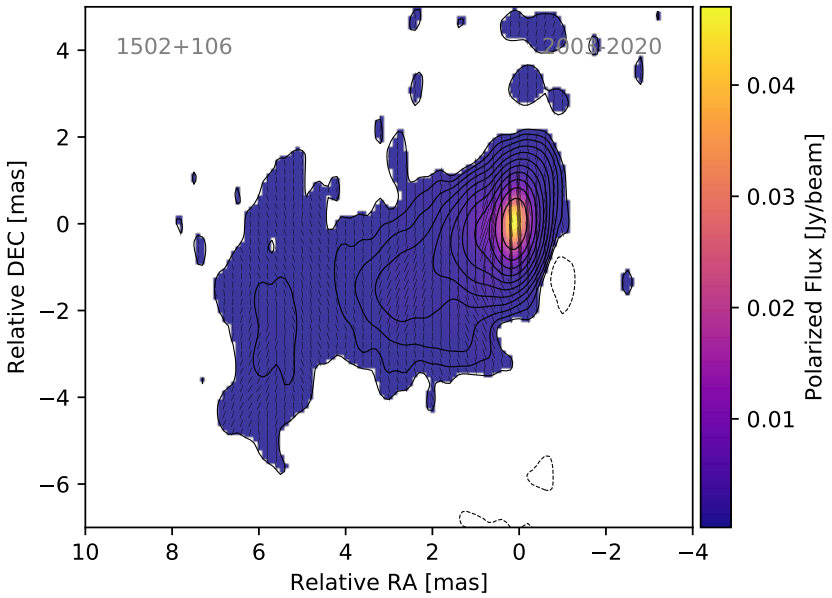

Figure 3.14.: Stacked total intensity image of PKS 1502+106 shown in contour lines overlayed with the stacked polarized image shown in color, together with the EVPAs. The stacked polarized image was produced with the 'P-EVPA-stack'-method as described in Section 2.3.

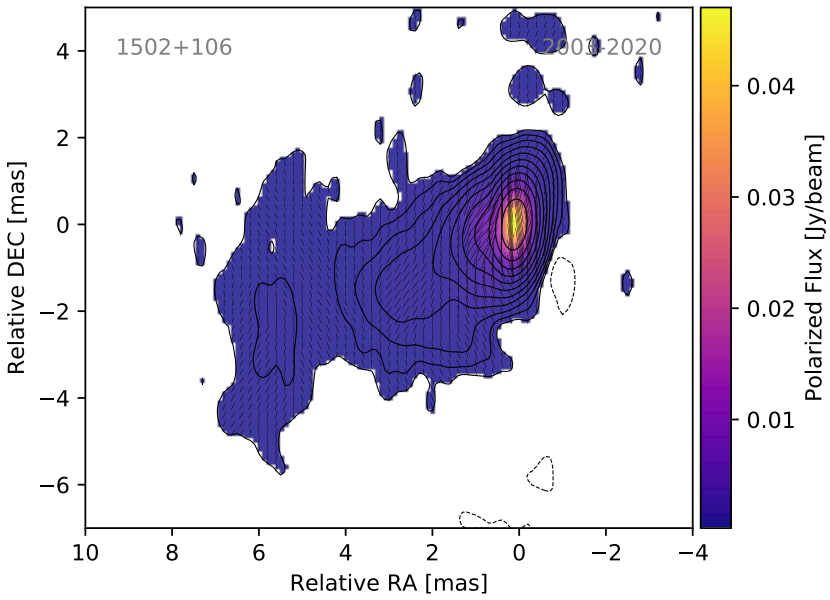

Figure 3.15.: Stacked total intensity image of PKS 1502+106 shown in contour lines overlayed with the stacked polarized image shown in color, together with the EVPAs. The stacked polarized image was produced with the 'P-EVPA-stack'-method as described in Section 2.3. Different to Figure 3.14, EVPAs are weighted with the polarized flux as their weights.

3.3.1. Spectral Index Maps

Additionally to the archival MOJAVE data of PKS 1502+106, an observation of this source obtained with the VLBA on 30 August 2019 was imaged. This observation contains data at 15 GHz, 24 GHz, and 43 GHz. For each band, a total intensity image was obtained with `DIFMAP` and can be seen in Figure 3.16. The corresponding image properties are listed in Table 3.1. All three images show a bright core with jet-like structure expanding east. The 43 GHz image shows a constriction with a following expansion of the jet at ~ 0.5 mas.

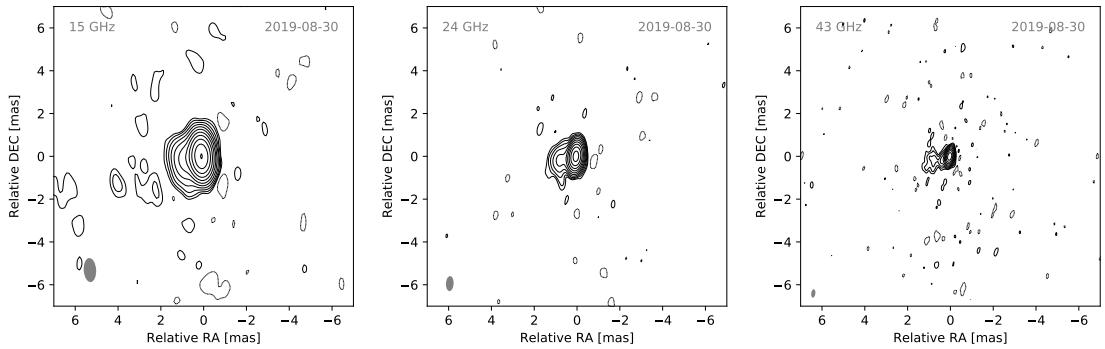

Figure 3.16.: PKS 1502+106 at 15 GHz, 24 GHz, and 43 GHz observed with the VLBA on 30 August 2019. The image properties are listed in Table 3.1.

Observation	S_{tot}	S_{peak}	σ_{rms}	b_{maj}	b_{min}	P.A
	[Jy]	[Jy/beam]	[mJy/beam]	[mas]	[mas]	[deg]
15 GHz	2.47	2.56	0.712	1.12	0.580	3.60
24 GHz	1.87	1.65	0.776	0.702	0.355	-2.98
43 GHz	0.735	0.577	0.446	0.395	0.189	-7.446

Table 3.1.: Image properties of the 15 GHz, 24 GHz, and 43 GHz observation of PKS 1502+106 with the VLBA on 30 August 2019. The corresponding images are shown in Figure 3.16.

The three images were used to obtain spectral index maps with the method described in Section 2.4. The spectral index map between 15 GHz and 24 GHz can bee seen in Figure 3.17 and between 24 GHz and 43 GHz in Figure 3.18. The corresponding image properties are listed in Table 3.2 and Table 3.3. In a first approach, the image with the smaller beam size was manipulated with `taper` and `restore` to bring the beam to the same size as in the other image. This is the most conservative

way since no beam smaller than the natural beam size is used. In Figure 3.17 and Figure 3.18, this approach can be seen on the top. A second approach was made with an intermediate beam lying between both beams. Here, the image with the bigger beam is slightly super-resolved. However, the beam sizes of the 15 GHz and the 24 GHz image, as well as the 24 GHz and the 43 GHz are not too different. In both cases, the smaller beam's major axis is more than half the size of the other beam.

The spectral index map between 15 GHz and 24 GHz shows a mostly flat core with a steeper optical thin component east of the core. The spectral index map between 24 GHz and 43 GHz shows patterns in the map that seem artificial. In the next chapter, a possible reason for these patterns is discussed.

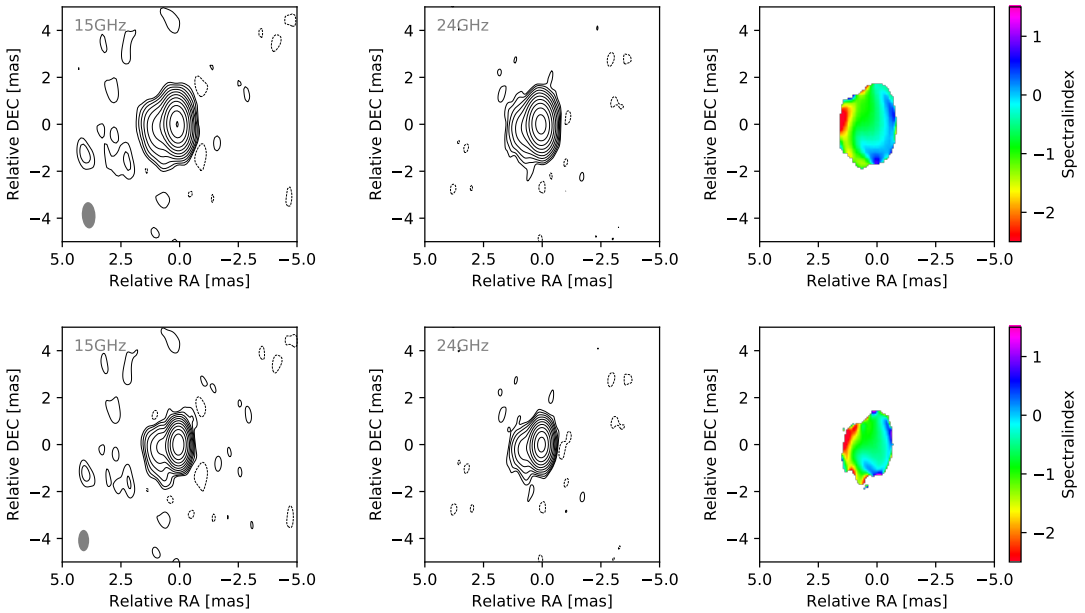

Figure 3.17.: Top: 15 GHz and 24 GHz image of PKS 1520+106. The 24 GHz image was convolved with the same beam as the 15 GHz image. On the right the corresponding spectral index map is shown. The map center and therefore also the source center has a spectral index of $\alpha_{center} = -0.547$. Bottom: Both images are convolved with an intermediate beam size. On the right the corresponding spectral index map is shown. The source center has a spectral index of $\alpha_{peak} = -0.616$. The corresponding image properties of all four images are listed in Table 3.2.

Observation	S_{tot} [Jy]	S_{peak} [Jy/beam]	σ_{rms} [mJy/beam]	b_{maj} [mas]	b_{min} [mas]	P.A [deg]
15 GHz	2.47	2.26	0.712	1.12	0.580	3.60
24 GHz	1.89	1.73	0.781	1.12	0.580	3.60
15 GHz	2.47	2.24	0.741	0.911	0.468	0.235
24 GHz	1.88	1.70	0.805	0.911	0.468	0.235

Table 3.2.: Image properties of the 15 GHz and 24 GHz images of PKS 1502+106 used to produce the spectral index maps shown in Figure 3.17. The first two rows correspond to the images with the bigger beam, the last two rows to the images with the intermediate beam.

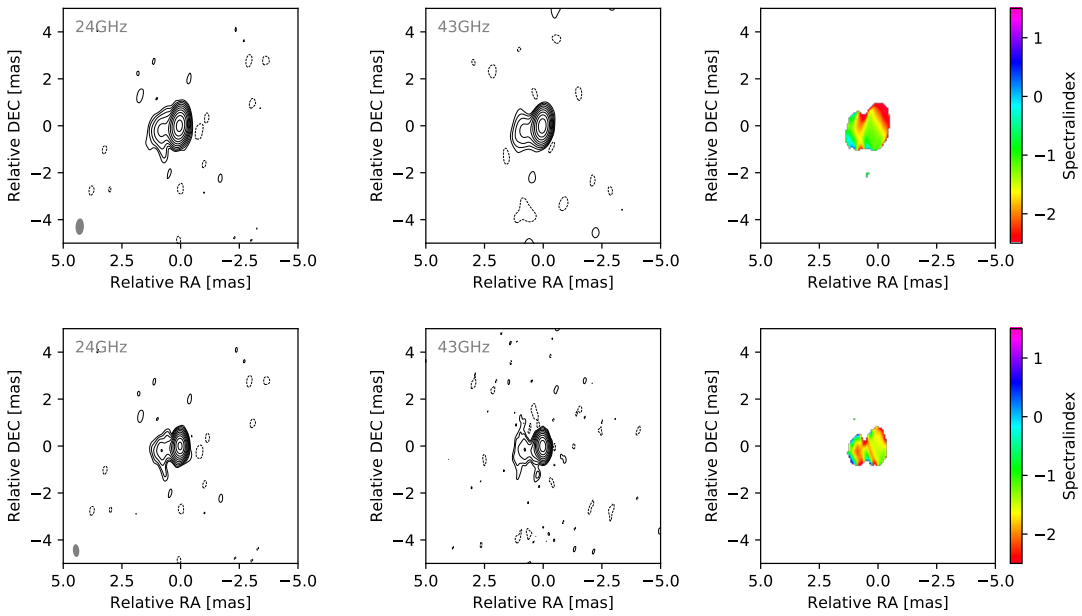

Figure 3.18.: Top: 24 GHz and 43 GHz image of PKS 1520+106. The 43 GHz image was convolved with the same beam as the 24 GHz image. On the right the corresponding spectral index map is shown. The map center and therefore also the source center has a spectral index of $\alpha_{peak} = -1.49$. Bottom: Both images are convolved with an intermediate beam size. On the right the corresponding spectral index map is shown. The source center has a spectral index of $\alpha_{peak} = -1.52$. The corresponding image properties of all four images are listed in Table 3.3.

Observation	S_{tot} [Jy]	S_{peak} [Jy/beam]	σ_{rms} [mJy/beam]	b_{maj} [mas]	b_{min} [mas]	P.A [deg]
24 GHz	1.84	1.65	0.776	0.702	0.355	-2.98
43 GHz	0.748	0.648	0.504	0.702	0.355	-2.98
24 GHz	1.87	1.56	0.798	0.547	0.272	4.91
43 GHz	0.730	0.624	0.493	0.547	0.272	4.91

Table 3.3.: Image properties of the 24 GHz and 43 GHz images of PKS 1502+106 used to produce the spectral index maps shown in Figure 3.18. The first two rows correspond to the images with the bigger beam, the last two rows to the images with the intermediate beam.

4. Discussion

The results presented in the last chapter are discussed in the following sections. This chapter's focus lies on the insights that a stacked total intensity image and a stacked polarized intensity image can yield. Furthermore, the three observed blazars are discussed regarding a possible spine-sheath structure and the associated neutrino production. Last, the obtained spectral index maps of PKS 1502+106 are analyzed.

Stacking Techniques

In this thesis, two stacking techniques are used: stacking total intensity images and the stacking of polarized images. The stacked total intensity image can give a good impression of a source's morphology, averaged over the period of time. As shown in the previous chapter, the stacked total intensity images of TXS 0506+056 and PKS 1502+106 show significant image artifacts. This behavior seems to be typical for stacked VLBI images: Small image artifacts resulting from the imaging process can appear in every epoch in the same place (for example in the north-south extension of the jet in TXS 0506+056). By stacking multiple images, these artifacts also get added up, and since they always appear in the same place, they do not cancel each other out like random noise. Therefore, the lowest contour line corresponding to a 3σ confidence level in the stacked image is not significantly lower than in the individual epochs. This would only be the case if the images only consist of the source and random noise.

In contrast to the stacked total intensity image, the stacked polarized images can reveal additional information. Both described methods (U-Q-stack and P-EVPA-stack) reveal the described trend of EVPAs being parallel to the jet in the spine and orthogonal in the outer parts. These connections are only partially visible in the single epochs. As shown, the trend of the EVPAs is reproduced in both methods with only slight differences. The main difference between both methods is reflected in the polarized intensity. While the U-Q-stack allows depolarization by stacking first all Stokes U and Q data, the P-EVPA-stack stacks all P values of the single

epochs. Therefore, in regions where the EVPAs change during the individual images, depolarization can take place. This can be best seen in PKS 1502+106 in Figure 3.14 and Figure 3.13. The region east of the core is in the U-Q-stack nearly as bright as the core, while in the P-EVPA-stack, the core is much brighter than this region. This leads to the conclusion that the polarization from the core undergoes more changes between the individual epochs. In contrast, EVPAs in the region east of the core are not changing much. Although this can also be seen in the single epoch images (see Appendix), the stacked polarized image can visualize these relationships in two single images directly comparable.

Spine-Sheath Model

All three observed blazars show at least in some epochs hints of limb brightening. For TXS 0506+056, this behavior is not unexpected since Ros et al. (2020) showed limb brightening in two observations. In the stacked total intensity image, limb brightening is also visible, which indicates that the source is often in this state.

PKS B1424-418 shows in several epochs limb brightening. Additionally, it is visible in the stacked total intensity image. Note that the observations of TXS 0506+056 range over eleven years, the observations of PKS B1424-418 only over five years.

Of all three sources, PKS 1506+106 shows the weakest hints of limb brightening. Only a few single epoch images show a jet that could be interpreted as limb brightened (see Figure 3.10 in the previous chapter). However, a more detailed analysis is needed to rule out any possibility of limb brightening.

The stacked polarized images of TXS 0506+056 and PKS 1502+106 show both EVPAs consistent with a spine-sheath model. In both sources, EVPAs tend to be parallel in the jet's center and gravitate towards an orthogonal orientation in the outer parts. These findings are consistent with the observations of Aaron (1999), who showed that the spine of the jet of Mrk 501 has magnetic field vectors orthogonal to the jet and the edges of the jet magnetic field vectors parallel to the jet. This behavior is again stronger in TXS 0506+056 than in PKS 1502+106.

In conclusion, hints of a spine-sheath structure are showing in all three sources, and the model could explain the neutrino flux of the blazars.

Spectral Index Maps

According to Marscher (2009), the core is the most compact part of the jet that can be imaged. This part could be the region transitioning from optically thick to thin emission or a bright and stationary structure downstream of that region. However, if the radio core is the region where the optical depth is near unity, the core's position depends on the observed frequency. At higher frequencies, the radio core is closer to the central engine.

To compensate for that, the positions of moving features of the jet can be measured in relation to the core. Because these features are optically thin, their position does not change at different frequencies. According to Lobanov (1998), the change in distance of these features to the core across different frequencies can then be used to compensate for the core shift.

In this thesis, no model-fitting of components in the jet was done, and therefore also no core shift was calculated. This can explain the spectral index maps of PKS 1502+106 presented in the previous chapter. Because the core shift is not compensated, the images for the spectral index image are slightly shifted. This can lead to the observed patterns in the spectral index that are prominent, especially in the 24 GHz-43 GHz spectral index image.

5. Summary and Outlook

In this thesis, VLBI observations of the blazars PKS B1424-418, TXS 0506+056, and PKS 1502+106 are presented. All three sources have strong associations to an IceCube neutrino event. From PKS B1424-418, ten TANAMI observations are imaged and stacked. The source shows a bright core with a jet expanding to the north-east. In some images the jet shows hints of limb-brightening, as well as in the stacked image.

TXS 0506+056 was studied by imaging all 24 archival MOJAVE observations that also contain polarization information. It also shows a bright core with a jet expanding south. Individual epochs, as well as the stacked total intensity image, show hints of limb-brightening, as confirmed by Ros et al. (2020). This supports a spine-sheath jet model proposed by Ghisellini et al. (2005) and Tavecchio et al. (2014) that could explain the neutrino output of these objects. TXS 0506+056 shows bright linear polarized intensity in the core. The jet shows in some epochs polarization. All polarization images are combined to a stacked polarized intensity image with two different methods. In the U-Q-stack, the individual Stokes U and Q data is stacked and then converted to P and EVPA. In the P-EVPA-stack, P and EVPA are calculated for each epoch and then stacked. The main difference between both methods is the possibility for depolarization in the U-Q-stack since U and Q are positive and negative, while P and EVPA are only positive.

In both methods, the EVPAs in the spine of the jet tend to be parallel to the jet and orthogonal in the outer parts. This is consistent with the observations of Aaron (1999) which construe this behavior to a spine-sheath structure in the jet.

Similar results were found by imaging 28 archival MOJAVE observations of PKS 1502+106. The source also shows a bright core and a jet expanding south-east. Compared to the other two sources, limb-brightening is only visible weakly in few episodes. Also, the stacked total intensity image shows no limb-brightening. However, the stacked polarized images indicate the same behavior of EVPAs as in TXS 0506+056, supporting a spine-sheath-model. Additionally, a single observation of PKS 1502+106 with the VLBA at 15 GHz, 24 GHz, and 43 GHz was studied and

spectral index maps between the three images calculated.

These spectral index maps could be improved by model-fitting and compensating for a core shift between the different frequencies. Model-fitting all images in this thesis could provide additional information about the blazars, such as the jet's opening angle and a comprehensive kinematic analysis. Furthermore, the hints of limb-brightening could be supported with the jets' surface brightness profiles for all available epochs, as presented in Ros et al. (2020).

With the ongoing search for extragalactic neutrinos, more and more possible neutrino sources should provide a clearer picture of the role AGN and their jets play in the mechanisms producing the neutrinos.

A. Single Epoch Images

Date	S_{tot}	S_{peak}	σ_{rms}	b_{maj}	b_{min}	P.A
YYYY-MM-DD	[Jy]	[Jy/beam]	[mJy/beam]	[mas]	[mas]	[deg]
2007-11-10	1.49	1.36	0.547	7.6	7.6	0
2008-03-28	1.68	1.52	0.925	7.6	7.6	0
2008-08-09	1.60	1.49	0.544	7.6	7.6	0
2009-02-23	1.22	1.08	0.911	7.6	7.6	0
2010-03-12	1.28	1.13	0.566	7.6	7.6	0
2010-07-24	1.29	1.20	0.438	7.6	7.6	0
2011-04-01	1.71	1.65	1.74	7.6	7.6	0
2011-11-13	2.13	1.94	1.01	7.6	7.6	0
2012-09-12	3.10	3.04	0.492	7.6	7.6	0
2013-03-14	6.23	6.06	1.54	7.6	7.6	0

Table A.1.: Image properties of the tapered images of PKS B1424-418 shown in Figure A.1.

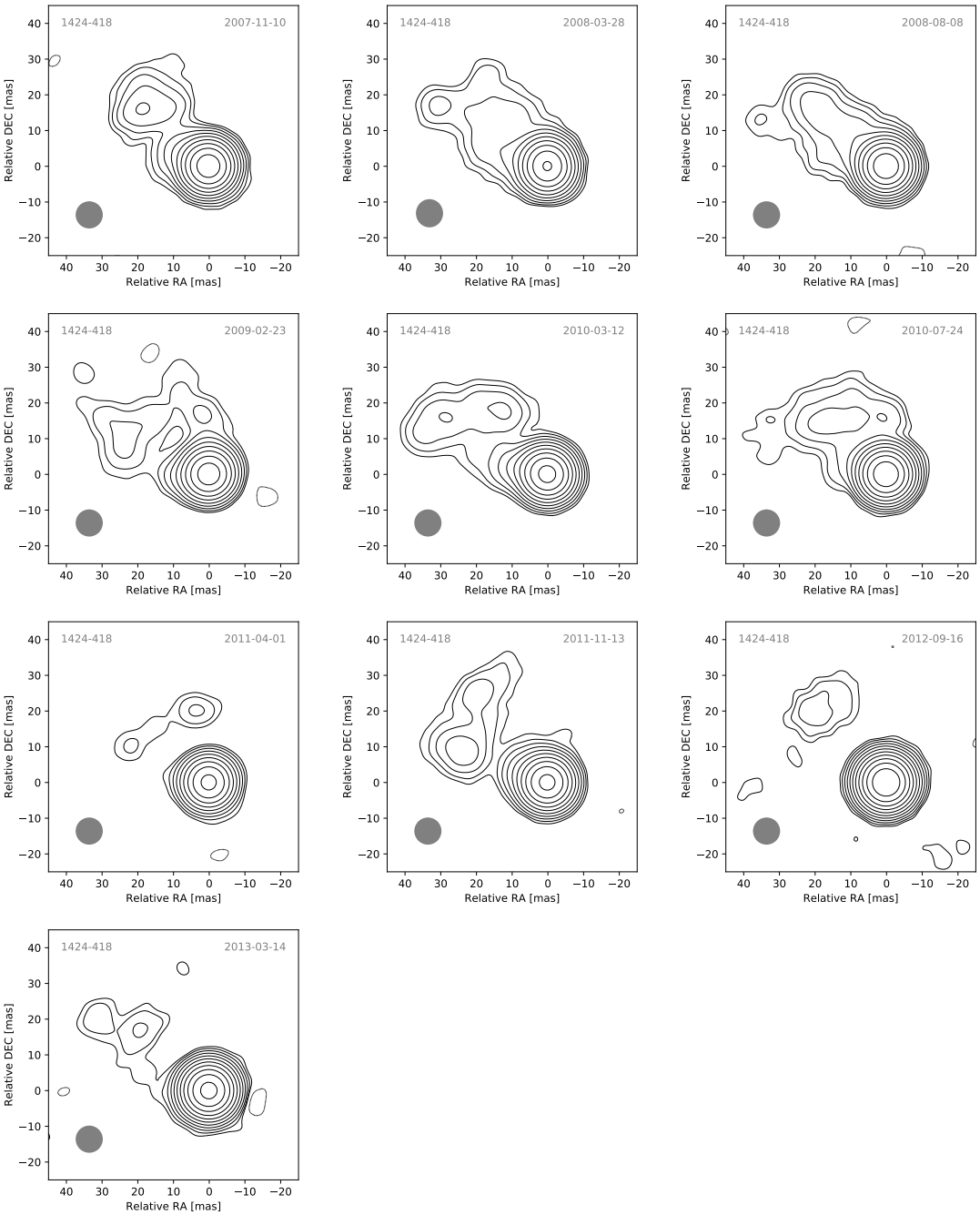

Figure A.1.: Tapered images of PKS B1424-418 obtained with TANAMI. The image properties are listed in Table A.1.

Date	S_{tot}	S_{peak}	σ_{rms}	b_{maj}	b_{min}	P.A
YYYY-MM-DD	[Jy]	[Jy/beam]	[mJy/beam]	[mas]	[mas]	[deg]
2007-11-10	1.47	1.03	0.237	2.12	0.523	4.23
2008-03-28	1.64	1.11	0.375	2.93	0.626	0.370
2008-08-09	1.58	1.41	0.508	3.45	1.59	-1.29
2009-02-23	1.11	0.818	0.346	1.27	1.08	17.3
2010-03-12	1.26	1.07	0.352	5.27	3.22	83.9
2010-07-24	1.25	0.921	0.358	2.77	0.705	14.3
2011-04-01	1.71	1.439	0.921	2.83	0.668	-8.69
2011-11-13	2.24	1.67	0.628	2.42	0.570	2.624
2012-09-12	3.09	2.81	0.606	2.04	0.627	4.48
2013-03-14	5.86	5.18	1.23	1.97	0.668	8.39

Table A.2.: Image properties of the full resolution images of PKS B1424-418 shown in Figure A.2.

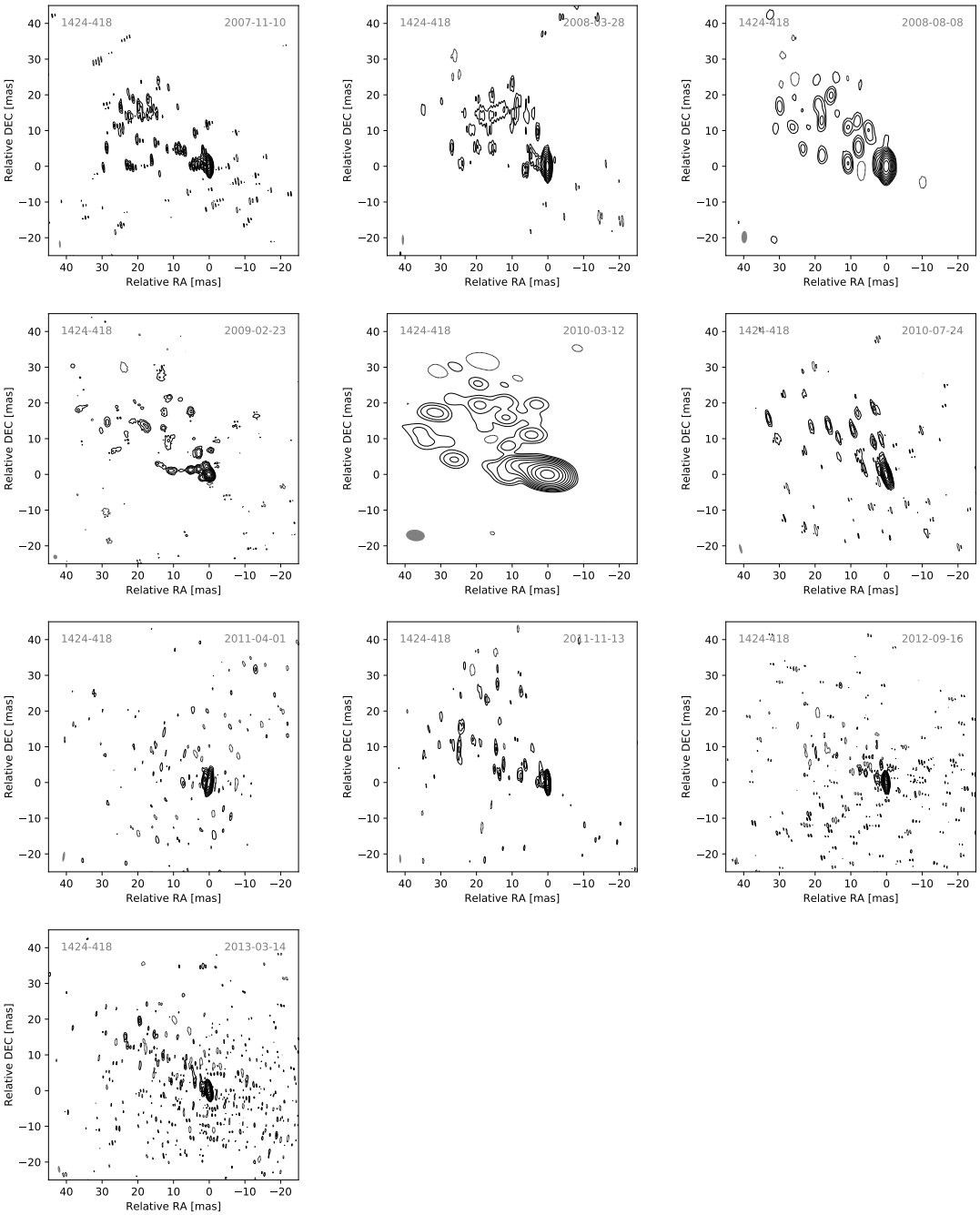

Figure A.2.: Full resolution images of PKS B1424-418 obtained with TANAMI. The image properties are listed in Table A.2.

Date	S_{tot}	S_{peak}	σ_{rms}	b_{maj}	b_{min}	P.A
YYYY-MM-DD	[Jy]	[Jy/beam]	[mJy/beam]	[mas]	[mas]	[deg]
2009-01-07	0.531	0.420	0.295	1.27	0.588	-2.53
2009-06-03	0.592	0.442	0.299	1.26	0.576	-3.68
2010-07-12	0.426	0.277	0.199	1.32	0.509	-6.63
2010-11-13	0.382	0.245	0.180	1.23	0.562	-5.68
2011-02-27	0.362	0.232	0.230	1.13	0.531	1.08
2012-02-06	0.339	0.236	0.180	1.20	0.556	-3.17
2013-02-28	0.323	0.238	0.221	1.18	0.540	-2.77
2014-01-25	0.422	0.312	0.184	1.16	0.557	-3.68
2015-01-18	0.424	0.301	0.212	1.25	0.519	-2.77
2015-09-06	0.387	0.271	0.153	1.18	0.503	-4.06
2016-01-22	0.308	0.212	0.159	1.22	0.531	-6.50
2016-06-16	0.448	0.320	0.122	1.14	0.514	-0.569
2016-11-18	0.531	0.405	0.170	1.15	0.525	-2.90
2017-06-17	0.590	0.454	0.186	1.15	0.497	-4.73
2018-04-22	0.905	0.715	0.266	1.17	0.519	-4.10
2018-05-31	0.991	0.796	0.302	1.15	0.504	-2.41
2018-12-16	1.04	0.843	0.266	1.19	0.561	3.78
2019-08-04	1.42	1.25	0.459	1.13	0.494	-3.51
2019-12-17	1.81	1.57	0.725	1.16	0.534	-3.19
2020-02-16	1.97	1.71	0.725	1.23	0.562	-3.77
2020-04-09	2.11	1.85	0.737	1.71	0.747	22.0
2020-05-08	2.13	1.81	1.52	1.27	0.592	-2.25
2020-06-13	1.85	1.49	0.769	1.21	0.506	-1.20
2020-08-01	1.82	1.44	0.760	1.217	0.540	1.49

Table A.3.: Image properties of the images of TXS 0506+056 shown in Figure A.3 and Figure A.4.

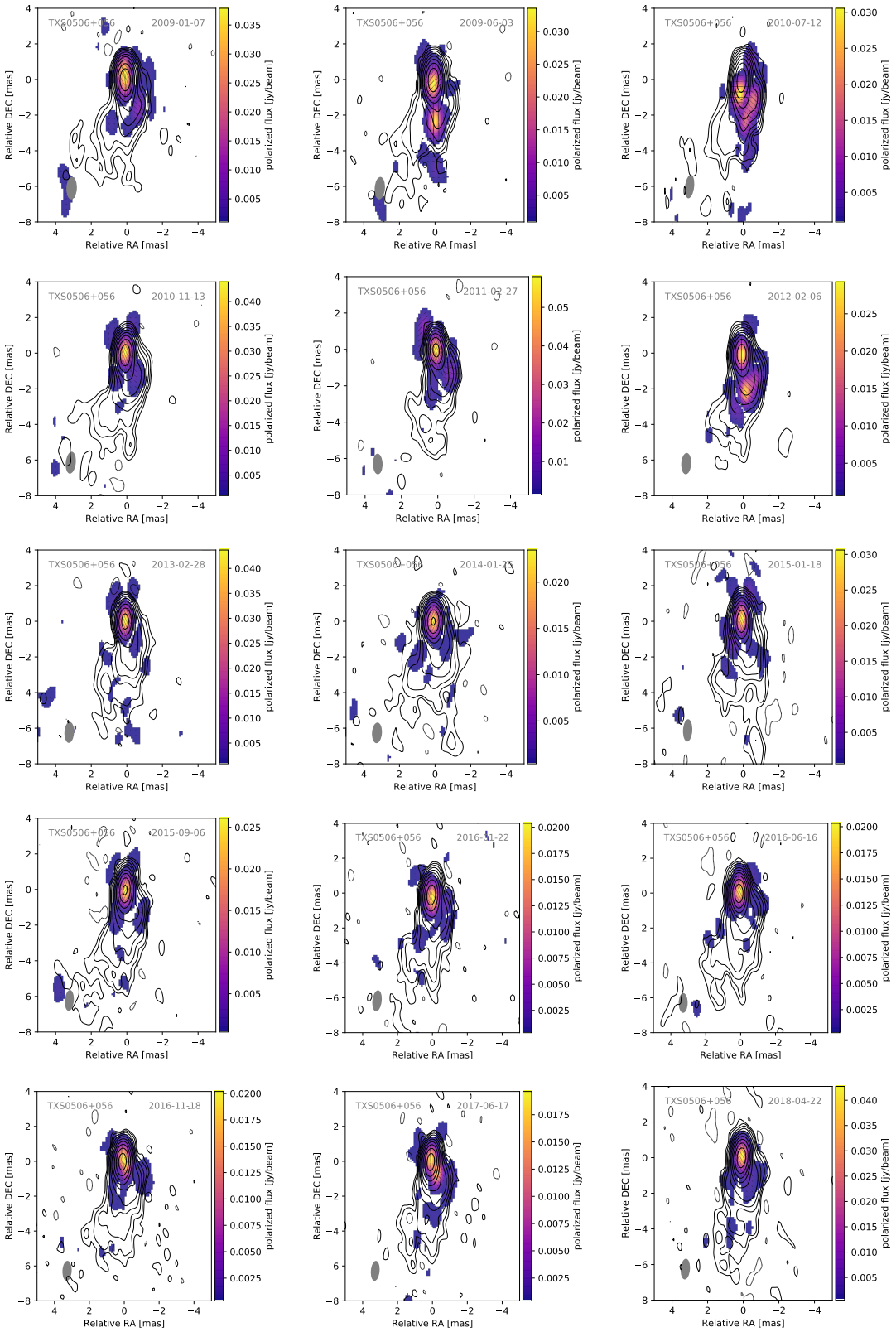

Figure A.3.: Images of TXS 0506+056. Shown is the full intesity image in contour lines and the polarized flux as a color map. The image properties are listed in Table A.3. Continued in Figure A.4.

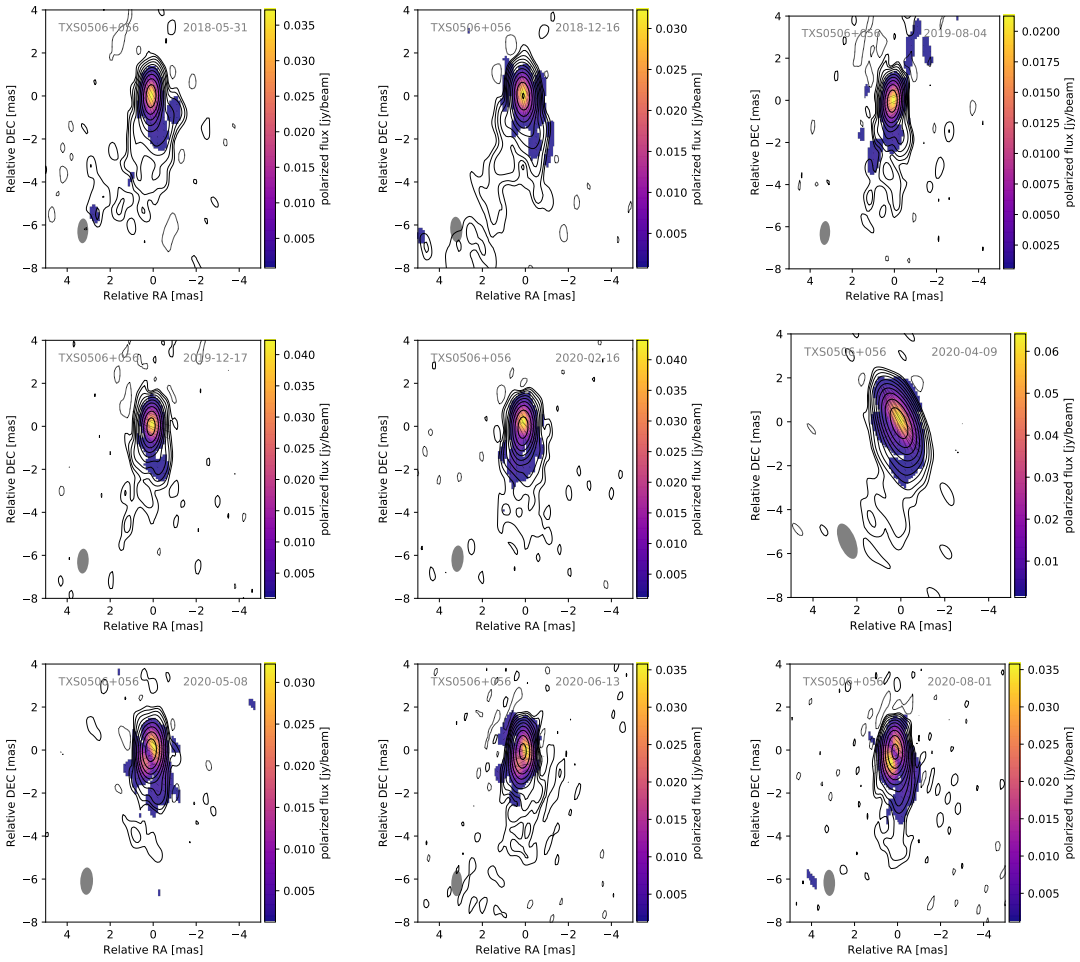

Figure A.4.: Continued: Images of TXS 0506+056. Shown is the full intesity image in contour lines and the polarized flux as a color map. The image properties are listed in Table A.3.

Date	S_{tot}	S_{peak}	σ_{rms}	b_{maj}	b_{min}	P.A
YYYY-MM-DD	[Jy]	[Jy/beam]	[mJy/beam]	[mas]	[mas]	[deg]
2003-03-29	1.82	1.37	0.481	1.11	0.532	0.540
2004-10-18	1.04	0.590	0.304	1.27	0.490	-10.3
2005-05-13	0.883	0.532	0.354	1.41	0.575	-12.4
2005-09-23	1.11	0.787	0.300	1.10	0.491	-2.16
2005-10-29	1.16	0.859	0.263	1.13	0.550	-5.36
2005-11-17	1.22	0.911	0.448	1.31	0.498	-9.90
2006-07-07	1.50	1.20	0.722	1.11	0.512	-6.34
2007-08-16	1.54	1.12	0.463	1.09	0.529	-6.21
2008-06-25	1.76	1.35	0.353	1.24	0.460	-8.18
2008-08-06	1.76	1.35	0.306	1.13	0.539	-6.23
2008-11-19	2.01	1.60	0.333	1.13	0.573	-2.62
2009-03-25	3.17	2.81	0.323	1.17	0.557	0.247
2009-12-10	1.51	1.20	0.216	1.12	0.571	-8.39
2010-06-19	1.01	0.720	0.166	1.21	0.563	-10.4
2010-06-27	0.977	0.737	0.321	1.16	0.492	-6.78
2010-08-27	1.01	0.742	0.171	1.10	0.510	-3.72
2010-11-13	1.14	0.870	0.160	1.15	0.512	-5.96
2011-02-27	1.26	0.988	0.201	1.08	0.510	1.30
2011-08-15	1.37	1.11	0.361	1.31	0.561	-1.28
2019-08-23	2.59	2.31	0.472	1.10	0.501	-9.12
2019-08-27	2.47	2.32	1.30	1.14	0.506	-7.58
2019-10-11	2.80	2.48	0.490	1.10	0.503	-1.33
2019-12-22	2.94	2.64	0.428	1.11	0.529	-2.66
2020-05-25	2.88	2.67	0.681	1.75	0.763	-15.7
2020-07-02	2.95	2.73	0.711	1.19	0.597	-0.564
2020-08-01	2.59	2.31	0.383	1.13	0.520	-1.70
2020-08-30	1.98	1.77	0.475	1.17	0.511	-4.08
2020-10-21	2.23	1.98	0.350	1.11	0.548	-3.30

Table A.4.: Image properties of the the images of PKS 1502+106 shown in Figure A.5 and Figure A.6.

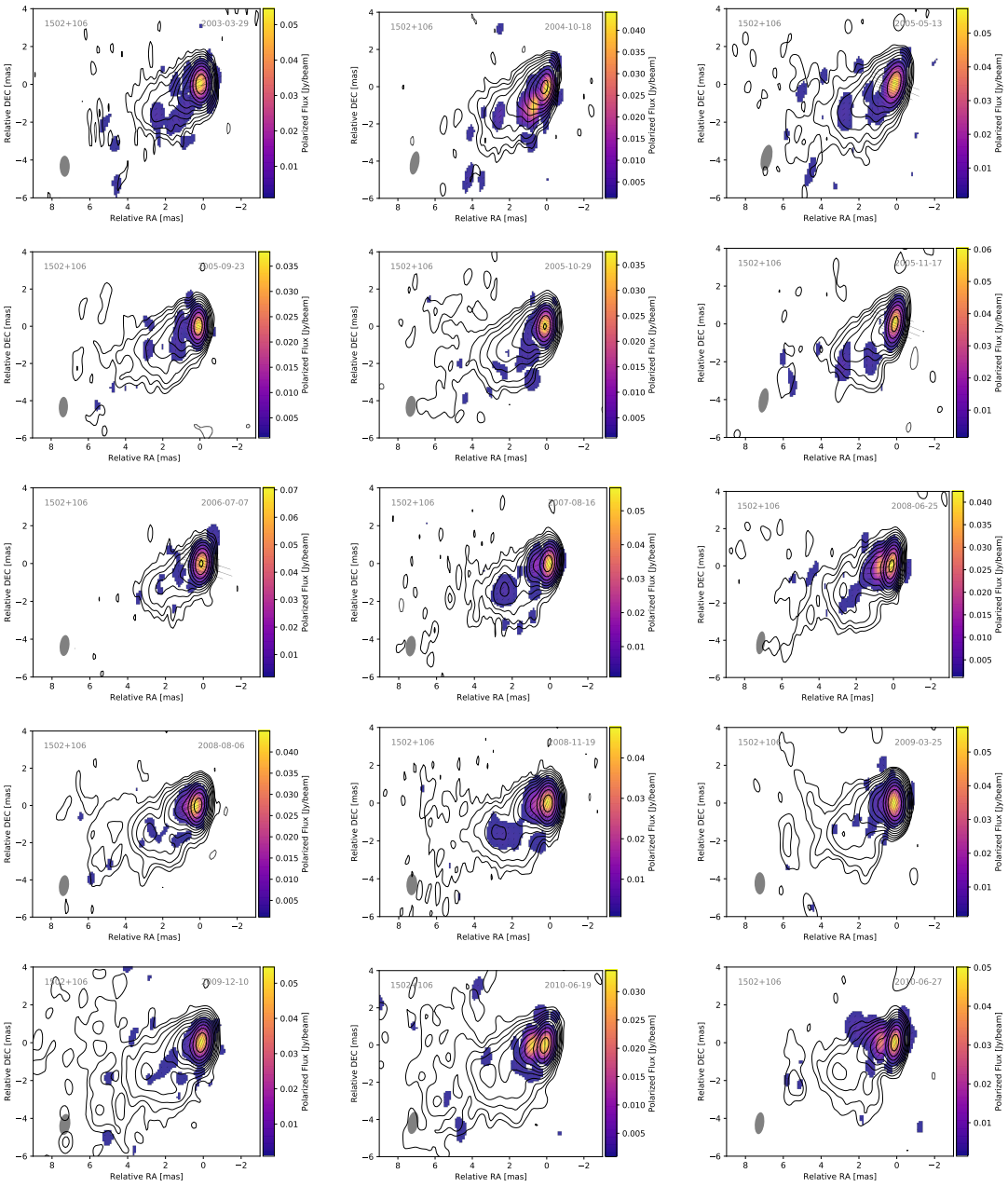

Figure A.5.: Images of PKS 1502+106. Shown is the full intesity image in contour lines and the polarized flux as a color map. The image properties are listed in Table A.4. Continued in Figure A.4.

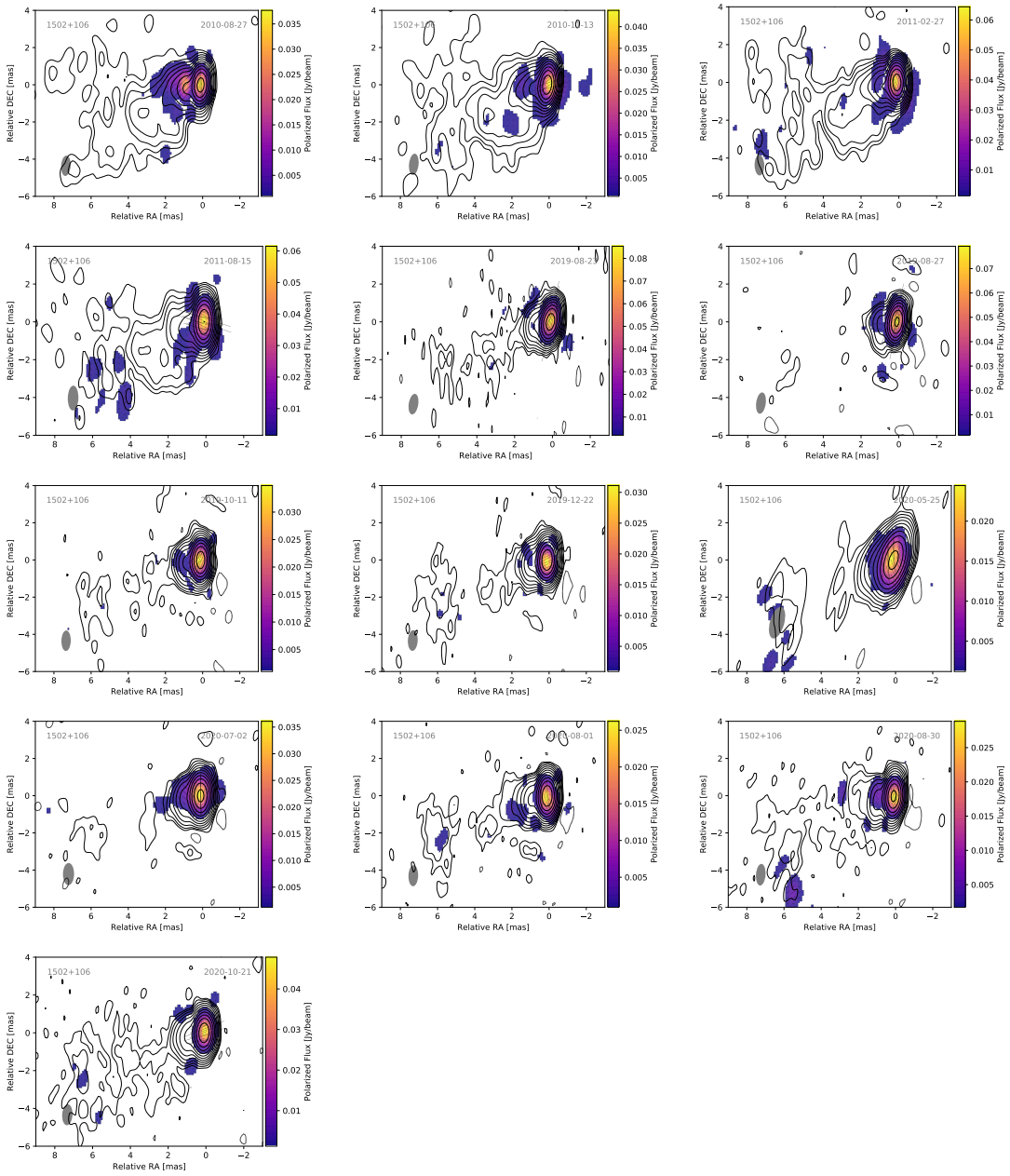

Figure A.6.: Continued: Images of PKS 1502+106. Shown is the full intesity image in contour lines and the polarized flux as a color map. The image properties are listed in Table A.4.

Bibliography

Aaron, Scott (1999). "VLBI Studies of MRK 501 and 0814+425". In: *BL Lac Phenomenon*. Vol. 159. Astronomical Society of the Pacific Conference Series, p. 427.

Aartsen, M. G. et al. (2014). "Observation of High-Energy Astrophysical Neutrinos in Three Years of IceCube Data". In: *Phys. Rev. Lett.* 113.10, 101101, p. 101101.

Aartsen, M. G. et al. (2017). "The IceCube Neutrino Observatory: instrumentation and online systems". In: *Journal of Instrumentation* 12.3, P03012.

Abdo, A. A. et al. (2010). "PKS 1502+106: A New and Distant Gamma-ray Blazar in Outburst Discovered by the Fermi Large Area Telescope". In: *ApJ* 710.1, pp. 810–827.

Abdo, A. A. et al. (2011). "Fermi Large Area Telescope Observations of Markarian 421: The Missing Piece of its Spectral Energy Distribution". In: *ApJ* 736, 131, p. 131.

Antonucci, R. (1993). "Unified models for active galactic nuclei and quasars". In: *ARA&A* 31, pp. 473–521.

Beckmann, V. and C. R. Shrader (2012). *Active Galactic Nuclei*.

Beuchert, T. et al. (2018). "VLBA polarimetric monitoring of 3C 111". In: *A&A* 610.

Britzen, S. et al. (2019). "A cosmic collider: Was the IceCube neutrino generated in a precessing jet-jet interaction in TXS 0506+056?" In: *A&A* 630, A103, A103.

Burd, P. R. (2017). "Long Wavelength Radio Observations of Blazars". Masters's Thesis. Julius-Maximilians-Universität Würzburg.

Burke, Bernard F. and Francis Graham-Smith (2009). *An Introduction to Radio Astronomy*.

Clark, B. G. (1999). "Coherence in Radio Astronomy". In: *Synthesis Imaging in Radio Astronomy II*. Vol. 180. Astronomical Society of the Pacific Conference Series, p. 1.

Cohen, M. H. et al. (2007). "Relativistic Beaming and the Intrinsic Properties of Extragalactic Radio Jets". In: *ApJ* 658.1, pp. 232–244.

Cornwell, Tim and Ed B. Fomalont (1999). "Self-Calibration". In: *Synthesis Imaging in Radio Astronomy II*. Vol. 180. Astronomical Society of the Pacific Conference Series, p. 187.

Curtis, H. D. (1918). "Descriptions of 762 Nebulae and Clusters Photographed with the Crossley Reflector". In: *Publications of Lick Observatory* 13, pp. 9–42.

Dermer, Charles D. et al. (2014). "Photopion production in black-hole jets and flat-spectrum radio quasars as PeV neutrino sources". In: *Journal of High Energy Astrophysics* 3, pp. 29–40.

Georganopoulos, Markos and Demosthenes Kazanas (2003). "Decelerating Flows in TeV Blazars: A Resolution to the BL Lacertae-FR I Unification Problem". In: *ApJ* 594.1, pp. L27–L30.

Ghisellini, G. et al. (2005). "Structured jets in TeV BL Lac objects and radiogalaxies. Implications for the observed properties". In: *A&A* 432.2, pp. 401–410.

Giovannini, G. et al. (1999). "VLBI Observations of Mrk421 and Mrk501". In: *BL Lac Phenomenon*. Vol. 159. Astronomical Society of the Pacific Conference Series, p. 439.

Giroletti, M. et al. (2004). "Parsec-Scale Properties of Markarian 501". In: *ApJ* 600.1, pp. 127–140.

Greisen, E. W. (2003). "AIPS, the VLA, and the VLBA". In: *Information Handling in Astronomy - Historical Vistas*. Vol. 285. Astrophysics and Space Science Library, p. 109.

Högbom, J. A. (1974). "Aperture Synthesis with a Non-Regular Distribution of Interferometer Baselines". In: *A&AS* 15, p. 417.

Hovatta, T. et al. (2020). "Association of IceCube neutrinos with radio sources observed at Owens Valley and Metsähovi Radio Observatories". In: *arXiv e-prints*.

IceCube Collaboration et al. (2018a). "Multimessenger observations of a flaring blazar coincident with high-energy neutrino IceCube-170922A". In: *Science* 361.6398.

IceCube Collaboration et al. (2018b). "Neutrino emission from the direction of the blazar TXS 0506+056 prior to the IceCube-170922A alert". In: *Science* 361.6398, pp. 147–151.

Jennison, R. C. (1958). "A phase sensitive interferometer technique for the measurement of the Fourier transforms of spatial brightness distributions of small angular extent". In: *MNRAS* 118, p. 276.

Kadler, M. et al. (2016). "Coincidence of a high-fluence blazar outburst with a PeV-energy neutrino event". In: *Nature Physics* 12.8, pp. 807–814.

Kellermann, K. et al. (1989). "VLA Observations of Objects in the Palomar Bright Quasar Survey". In: *AJ* 98, p. 1195.

Kellermann, K. et al. (1998). "Sub-Milliarcsecond Imaging of Quasars and Active Galactic Nuclei". In: *AJ* 115.4, pp. 1295–1318.

Kiehlmann, S. et al. (2019). "Neutrino candidate source FSRQ PKS 1502+106 at highest flux density at 15 GHz". In: *The Astronomer's Telegram* 12996, p. 1.

Krawczynski, H. et al. (2002). "Time-dependent modelling of the Markarian 501 X-ray and TeV gamma-ray data taken during 1997 March and April". In: *MNRAS* 336.3, pp. 721–735.

Lister, M. L. and D. C. Homan (2005). "MOJAVE: Monitoring of Jets in Active Galactic Nuclei with VLBA Experiments. I. First-Epoch 15 GHz Linear Polarization Images". In: *AJ* 130.4, pp. 1389–1417.

Lister, M. L. et al. (2009). "MOJAVE: Monitoring of Jets in Active Galactic Nuclei with VLBA Experiments. V. Multi-Epoch VLBA Images". In: *AJ* 137.3, pp. 3718–3729.

Lobanov, A. P. (1998). "Ultracompact jets in active galactic nuclei". In: *A&A* 330, pp. 79–89.

Marscher, A. P. (2009). "Jets in Active Galactic Nuclei". In: *arXiv e-prints*.

Murase, Kohta et al. (2014). "Diffuse neutrino intensity from the inner jets of active galactic nuclei: Impacts of external photon fields and the blazar sequence". In: *Phys. Rev. D* 90.2, 023007.

Ojha, R. et al. (2010). "TANAMI: tracking active galactic nuclei with austral milliarcsecond interferometry . I. First-epoch 8.4 GHz images". In: *A&A* 519, A45, A45.

Padovani, P. and E. Resconi (2014). "Are both BL Lacs and pulsar wind nebulae the astrophysical counterparts of IceCube neutrino events?" In: *MNRAS* 443.1, pp. 474–484.

Pearson, T. J. and A. C. S. Readhead (1984). "Image Formation by Self-Calibration in Radio Astronomy". In: *ARA&A* 22, pp. 97–130.

Richards, Joseph L. et al. (2011). "Blazars in the Fermi Era: The OVRO 40 m Telescope Monitoring Program". In: *ApJS* 194.2, 29, p. 29.

Ros, E. et al. (2020). "Apparent superluminal core expansion and limb brightening in the candidate neutrino blazar TXS 0506+056". In: *A&A* 633, L1.

Rybicki, G. B. and A. P. Lightman (1979). *Radiative processes in astrophysics*.

Salpeter, E. E. (1964). "Accretion of Interstellar Matter by Massive Objects." In: *ApJ* 140, pp. 796–800.

Seyfert, Carl K. (1943). "Nuclear Emission in Spiral Nebulae." In: *ApJ* 97, p. 28.

Shepherd, M. C. (1997). "Difmap: an Interactive Program for Synthesis Imaging". In: *Astronomical Data Analysis Software and Systems VI*. Vol. 125. Astronomical Society of the Pacific Conference Series, p. 77.

Taboada, Ignacio and Robert Stein (2019). "IceCube-190730A an astrophysical neutrino candidate in spatial coincidence with FSRQ PKS 1502+106". In: *The Astronomer's Telegram* 12967, p. 1.

Tavecchio, Fabrizio and Laura Maraschi (2001). "Constraints to the SSC model for Mkn 501". In: *X-ray Astronomy: Stellar Endpoints, AGN, and the Diffuse X-ray Background*. Vol. 599. American Institute of Physics Conference Series, pp. 979–982.

Tavecchio, Fabrizio et al. (2014). "Structured Jets in BL Lac Objects: Efficient PeV Neutrino Factories?" In: *ApJ* 793.1, L18.

Thompson, A. Richard et al. (2017). *Interferometry and Synthesis in Radio Astronomy, 3rd Edition*.

Urry, C. M. and P. Padovani (1995). "Unified Schemes for Radio-Loud Active Galactic Nuclei". In: *PASP* 107, p. 803.

Walker, R. Craig et al. (2018). "The Structure and Dynamics of the Subparsec Jet in M87 Based on 50 VLBA Observations over 17 Years at 43 GHz". In: *ApJ* 855.2, 128, p. 128.

Walt, Stéfan van der et al. (2014). "scikit-image: image processing in Python". In: *PeerJ* 2, e453.

Weber, P. (2020). "VLBI Properties of Candidate Neutrino-Emitting Blazars". Bachelor's Thesis. Julius-Maximilians-Universität Würzburg.

White, Graeme L. et al. (1988). "Redshifts of Southern Radio Sources. VII." In: *ApJ* 327, p. 561.

Acknowledgments

I want to thank everyone who supported me during the process of working on this thesis and contributed to its success.

First and foremost, I would like to thank Prof. Dr. Matthias Kadler for giving me the opportunity to work on this thesis. I am thankful for his continuous supervision and many productive discussion during my time in the Department of Astronomy. His class raised my interest in extragalactic jets and the exploration of them via VLBI. Furthermore, I would also like to thank Prof. Dr. Karl Mannheim, chair holder of the astronomy department in Würzburg, for the opportunity to complete my Master's Degree there. Prof. Dr. Eduardo Ros was a great help as a MOJAVE expert regarding the polarized images. Many video conferences with him and Prof. Dr. Matthias Kadler helped me with my thesis, and I want to thank him for that. I want to thank Tobias Beuchert for his assistance with all stacking techniques and polarized images. Marcus Langejahn was teaching me how to use ISIS, and I thank him for that.

Furthermore, I want to thank everyone who helped me writing this thesis with constructive feedback, encouragement, and proofreading. Namely Andreas Gokus, Paul Ray Burd, Florian Rösch, Jonas Sinapius, and Florian Eppel. Additionally, I would like to thank everyone else in the Department of Astronomy in Würzburg for always providing a productive work environment.

A special thanks to my family, who made my studies possible and always supported me in my decisions. And to Antonia, who encouraged me the whole time and who is always there for me.

This research has made use of data from the OVRO 40-m monitoring program (Richards, J. L. et al. 2011, ApJS, 194, 29) which is supported in part by NASA grants NNX08AW31G, NNX11A043G, and NNX14AQ89G and NSF grants AST-0808050 and AST-1109911.

This research has made use of data from the MOJAVE database that is maintained by the MOJAVE team (Lister et al., 2018, ApJS, 232, 12).

Declaration of authorship

I, Luis Wachter, hereby decline that I am the sole author of this thesis. I have not used any sources other than those listed and made it clear when I have consulted the work of others. This thesis was not submitted at any other institution before.

Place, Date Signature